PNIPAM HYDROGEL MICRO/NANOSTRUCTURES FOR BULK FLUID AND DROPLET CONTROL

A Thesis
Presented to
The Academic Faculty

by

James Emanuel Silva

In Partial Fulfillment
of the Requirements for the Degree
Master of Science in the
School of Mechanical Engineering

Georgia Institute of Technology
December 2014

PNIPAM HYDROGEL MICRO/NANOSTRUCTURES FOR BULK FLUID AND DROPLET CONTROL

Approved by:

Dr. Andrei G. Fedorov, Advisor
School of Mechanical Engineering
Georgia Institute of Technology

Dr. Peter A. Kottke
School of Mechanical Engineering
Georgia Institute of Technology

Dr. Cyrus K. Aidun
School of Mechanical Engineering
Georgia Institute of Technology

Date Approved: July 29, 2014

ACKNOWLEDGEMENTS

Success in this research project would not have been possible with the discussions and support provided by numerous colleagues, friends, and family. First and foremost, I would like to thank my advisor, Dr. Andrei Fedorov for his unfaltering enthusiasm. Going above and beyond, Dr. Fedorov has modeled what it means not only to be an excellent scientist, but a great mentor. I would also like to express my gratitude to Dr. Peter Kottke, whose willingness to meet with me anytime I felt lost helped me to stay on track and keep sight of what I was working towards.

I was fortunate enough to be a part of the MITf lab group here at Georgia Tech, and I appreciate all the experience and advice my lab mates were willing to share. In particular, I would like to acknowledge the roles that Drew Loney and David Anderson played in advancing the progress of this Master’s research. Likewise, I am very grateful for the support of Dr. Vladimir Tsukruk, Ren Geryak, and all the other members of the Surface Engineering and Molecular Assembly lab group whose knowledge of polymer systems helped bring me up to speed with a research field I initially knew nothing about.

Of course, I would like to thank my parents for their ongoing support in my studies and decision to pursue my Master’s degree. I also extend a very special thank you to Tanya Liu, whose many phone calls helped the treks across campus and between labs to go by that much faster.

Finally, I would like to acknowledge the Institute of Paper Science and Technology at Georgia Tech for my Paper Science Fellowship, and financial support from the U.S. Air Force Office of Scientific Research.

TABLE OF CONTENTS

LIST OF TABLES

LIST OF FIGURES

LIST OF SYMBOLS AND ABBREVIATIONS

$a(t)$	Distance from capillary center to deformed gel
D	Diffusivity
d	Capillary inner diameter
J	Mass flux of water into hydrogel
L	Lateral deformation length beyond contact line
L_{pipe}	Pipe length
l_e	Hydrodynamic entry length
$\dot{Q}$	Volumetric flow rate
R	Capillary radius
t	Time
x_{m}	Meniscus position
γ	Surface tension
ΔP	Pressure drop
δ	swollen gel thickness
θ_{m}	meniscus contact angle
θ_{gel}	Angle of gel deformation beyond the contact line
θ^*	Complement of θ_{m}
μ	Dynamic viscosity
φ_{i}	Initial state volume fraction of water in hydrogel
φ_{sw}	Swollen state volume fraction of water in hydrogel
AFM	Atomic Force Microscopy
APS	Ammonium Persulfate

FPS	Frames Per Second
ID	Inner Diameter
LCST	Lower Critical Solution Temperature
MBA	*N*,*N'*-Methylenebisacrylamide
PNIPAM	Poly-*N*(isopropylacrylamide)
Re	Reynolds Number
SEM	Scanning Electron Microscope
TEMED	Tetramethylethylenediamine
VTMS	Vinyltrimethoxysilane

SUMMARY

Within the field of polymers, a sub-group known as stimuli-responsive or “smart” polymers has emerged in recent years. Such polymers have the inherent ability to exhibit conformational changes in response to external stimuli such as temperature, pH, and electric/magnetic fields. By combining an autonomous sensing/actuation mechanism into a single material, “smart” polymers have generated enormous research interest and are ubiquitous in their application across various fields.

This thesis examines the unique interactions that occur when PNIPAM, a prominent temperature-responsive polymer, is cast in hydrogel form at the micro and nanoscales. The primary focus is a target system which features a PNIPAM coating synthesized along the inner diameter of a capillary. A series of experiments investigate how swelling of PNIPAM hydrogel layers gives way to complex contact line dynamics that result in significant contact line pinning along the hydrogel for fluid flow through the coated capillary. As simple fluid flow models fail to capture the effect of the swelling gel interface, an analytical framework is proposed that builds upon experimental observations and describes the relationship between swelling and pinning.

Additional exploratory work highlights different attempts at fabricating nanopillar arrays from PNIPAM hydrogels. These attempts focus on use of porous alumina membranes as templates in which gel precursor solution can be introduced an cured, with the template structure dissolved to reveal nanopillars. Lessons learned are highlighted and a recommended course of next steps is provided.

CHAPTER 1

INTRODUCTION

Stimuli-responsive polymers represent an exciting material class whose unique properties are well suited for tackling a wide range of research challenges. Part of their appeal is the unique manner in which these polymers combine functionality, simultaneously serving as both threshold sensors and actuator. These smart polymers have become quite ubiquitous in today's research fields, and show promising growth for both research and commercial applications.

This first section provides an introduction to poly(*N*-isopropylacrylamide) (PNIPAM), a well-studied polymer demonstrating temperature-responsiveness. Several factors guided the choice of PNIPAM for this research project. First and foremost, temperature is an important stimulus for processes ranging across many fields, and typically must be controlled so as not to exceed threshold values. Although this work focuses on more fundamental research aspects and did not feature a target application, the results can be generalized to many instances in which temperature is an important stimulus. Another important factor that guided the choice of PNIPAM was its prominence in literature. This is especially important to consider in the case of modeling the hydrogel swelling process, in which specific parameters are needed. Finally, PNIPAM is commonly cast in a variety of forms including brushes, micro/nanogels, and films, allowing for flexible integration dictated by specific applications.

This section serves as a brief introduction to the key characteristics of PNIPAM. The nature of its temperature induced phase transition is explained, and examples of applications are used to briefly illustrate the polymer's practical utility. Some background is then provided for thermodynamic modeling a swelling hydrogel, and the chapter concludes with a review of recent literature concerning wetting of hydrogels.

1.1 Poly(*N*-isopropylacrylamide): Characteristics and Applications

Poly(*N*-isopropylacrylamide), typically referred to as PNIPAM, is a stimuli responsive, "smart" polymer that has been extensively studied due to its ability to respond to solution temperature. When heating solution temperature above the lower critical solution temperature (LCST), PNIPAM shows reversible chain collapse as it becomes thermodynamically more favorable for the polymer to associate with itself than with water. As demonstrated in Figure 1a, this means that PNIPAM chains dissolved in solution will spontaneously phase separate as temperature increases beyond this threshold. By chemically bonding many PNIPAM chains together to form a three-dimensional array, a hydrogel is formed, and this phase separation behavior manifests itself as temperature-induced volume changes. Below LCST, PNIPAM hydrogels exhibit hydrophilic behavior by imbibing water to form swollen gel networks. As with the case of individual PNIPAM chains, heating PNIPAM hydrogels above their LCST causes them to take on a more hydrophobic nature, spontaneously expelling water and shrinking (Figure 1b).

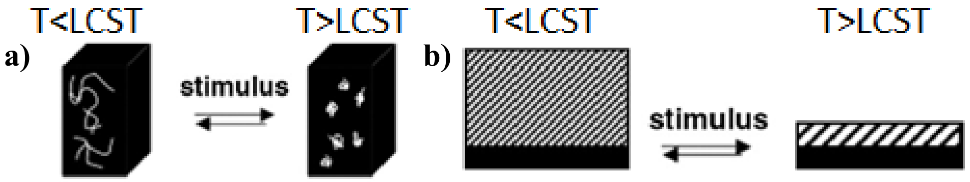

Figure 1: Two different manifestations of heating PNIPAM above LCST. (a) Below LCST, PNIPAM chains exist in an extended, hydrated state before collapsing in on themselves above LCST. (b) PNIPAM hydrogels expel water upon heating above LCST, resulting in a shrunken state [1].

PNIPAM's LCST is typically quoted in the range of 31-34°C, as it varies within a few degrees based on the content of NIPAM monomer and the crosslinking density. To shift the LCST beyond this small range, Figure 2 demonstrates how copolymerizing NIPAM with non-responsive monomers allows the LCST to linearly increase with decreasing PNIPAM content (labeled as PAm in the figure). While copolymerization allows for modulation of other hydrogel properties such as swelling capacity, it can also be utilized to integrate additional responsiveness to stimuli beyond temperature. Examples include copolymerization of NIPAM with pH sensitive monomers for dual temperature/pH swelling responses [2, 3], as well as temperature/electromagnetic field responsive copolymers [4-6].

The appeal of temperature induced actuation has enabled integration of PNIPAM hydrogels into a wide variety of applications spanning many fields. Given the similarity of PNIPAM's LCST (32°C) to the human body temperature (37°C), a prominent research area has been in utilizing PNIPAM for controlled drug delivery [7-9]. Such applications differ in their implementation, but typically feature some drug-load core with a PNIPAM shell controlling the diffusion of drug particles into the human body (Figure 3a). In microfluidics, applications such as lab-on-a-chip have utilized the temperature sensitive properties of the hydrogel to create "smart" valves [10-12] that autonomously open and

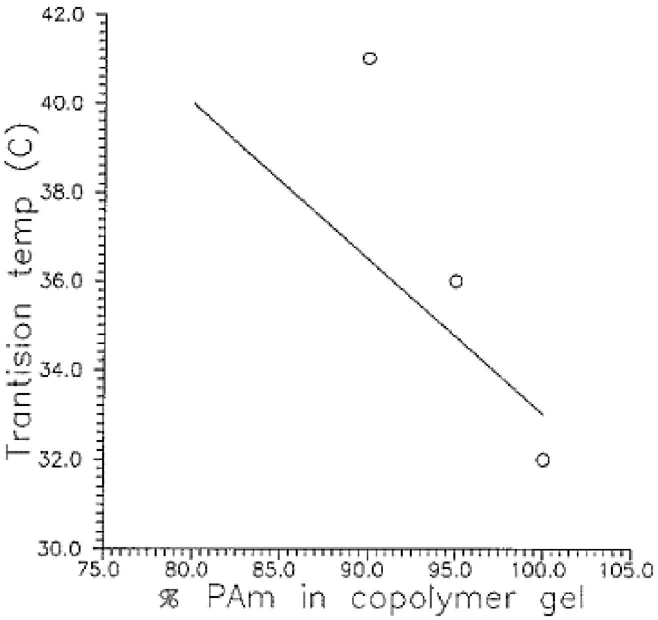

Figure 2: By copolymerizing NIPAM with non-temperature responsive polymers, it is possible to increase shift the polymer's transition temperature (LCST). The solid line represents a qualitative prediction of this effect, compared with experimental data [13].

close based on solution temperature (Figure 3b). Other applications areas for PNIPAM include generalized actuators [14, 15], sensors [16, 17], and surfaces with controlled protein/cell adsorption [18].

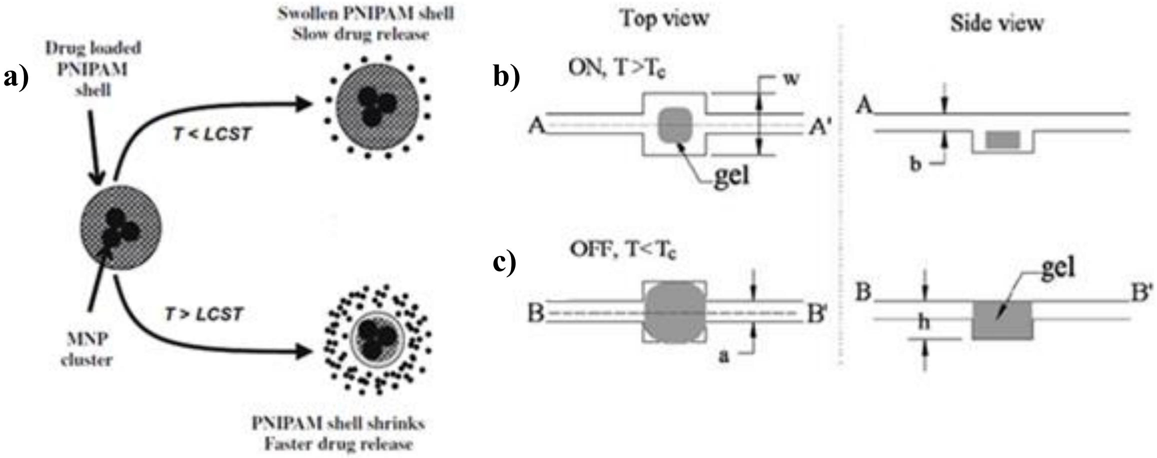

Figure 3: Examples of PNIPAM applications. (a) As temperature increases, the PNIPAM shell shrinks, squeezing out the drug particles [8]. (b) PNIPAM hydrogel integrated as a microfluidic valve. As temperature of the passing stream falls below LCST (c), the gel swells and prevents flow [19].

1.2 Thermodynamics of PNIPAM Hydrogels

Consider a unit of hydrogel, initially devoid of water, that is suddenly immersed in a reservoir of water. The chemical potential for water in the dry hydrogel is μ_0, while the reservoir is at temperature T (T < LCST) and has a chemical potential μ. Since the initial chemical potential for water in the hydrogel (μ_0) is less than that of the bulk water (μ), water begins diffusing from the bulk into the hydrogel. As this occurs, the polymer network begins to deform, giving rise to swelling. A typical assumption of hydrogel thermodynamics is that both the polymer and water are considered incompressible; hence, the increase in hydrogel volume during swelling is exactly equal to the volume of imbibed water.

As the hydrogel begins swelling, it can be considered a composite system composed of polymer and imbibed water. The change in free energy of this system has two components: an elastic term and a mixing term. To model changes in the hydrogel's elastic energy, the polymer is modeled as a Neo-Hookean material. Like a deformed spring, stretching the polymer allows it to store energy; following a derivation from Flory [20], this is typically taken as

$$W_{\text{elas}} = 0.5NkT\left[\lambda_1^2\lambda_2^2\lambda_3^2 - 3 - 2\ln(\lambda_1\lambda_2\lambda_3)\right] \qquad 1$$

where k is the Boltzmann constant, N is the crosslinking density (number of crosslinks per unit volume of dry gel), and λ is the stretch ratio (ratio of deformed length to initial length for each of the three principle directions).

Free energy changes associated with mixing capture the different interaction energies between molecules. With the onset of swelling, water molecules begin entering the polymer network and pure polymer/polymer interactions give way to a mixture of polymer/polymer, water/water, and water/polymer interactions. The configurational energy of water molecules with monomer units, combined with these nearest neighbor interactions, gives [20]

$$W_{\mathrm{mix}} = RT\left[n_{\mathrm{w}} \ln \varphi_{\mathrm{w}} + n_{\mathrm{p}} \ln \varphi_{\mathrm{p}} + n_{\mathrm{w}}\varphi_{\mathrm{p}}\chi_{\mathrm{w-p}}\right] \qquad 2$$

where the w/p subscripts denote water and polymer, R is the universal gas constant, n is the number of moles, φ is the volume fraction, and χ is the Flory-Huggins interaction parameter, characterizing the energy of interdispersing water and polymer molecules.

Adding the elastic and mixing free energy components and plotting the results, Figure 4a displays representative free energy isotherms as a function of the swelling ratio (i.e., ratio of swollen volume to dry polymer volume). Figure 4b, in turn, is formed by collecting the loci of all local maxima and minima from the free energy isotherms. Classical thermodynamics dictates that a system will always seek to assume its lowest *attainable* energy state. However, from Figure 4b, it is apparent that in the temperature range of approximately 304.7-305.7K, there exist two stable equilibrium points (local minima) separated by an unstable equilibrium (local maximum).

Consider now the case of cooling solution temperature from 306K to 304K. At 306K, Figure 4a shows only one local minimum, which corresponds to the hydrogel's equilibrium state at this temperature. Reducing the temperature to 305K, two equilibrium points exist- one at $\mathrm{V}/\mathrm{V}_0 \approx 1.5$, and one at $\mathrm{V}/\mathrm{V}_0 = 7$. Energetically, the equilibrium state corresponding to $\mathrm{V}/\mathrm{V}_0 = 7$ is preferred since it represents a lower energy state. However, this equilibrium state is unattainable as it requires an energy input in order to surpass the local maximum (i.e., energy barrier) at $V/V_0 = 2$. Thus, when cooling solution temperature, the hydrogel's equilibrium configuration at 305K corresponds to $V/V_0 = 1.5$. Continuing on to 304K, again, only one extremum is present, thereby defining the hydrogel's equilibrium state when further reducing solution temperature.

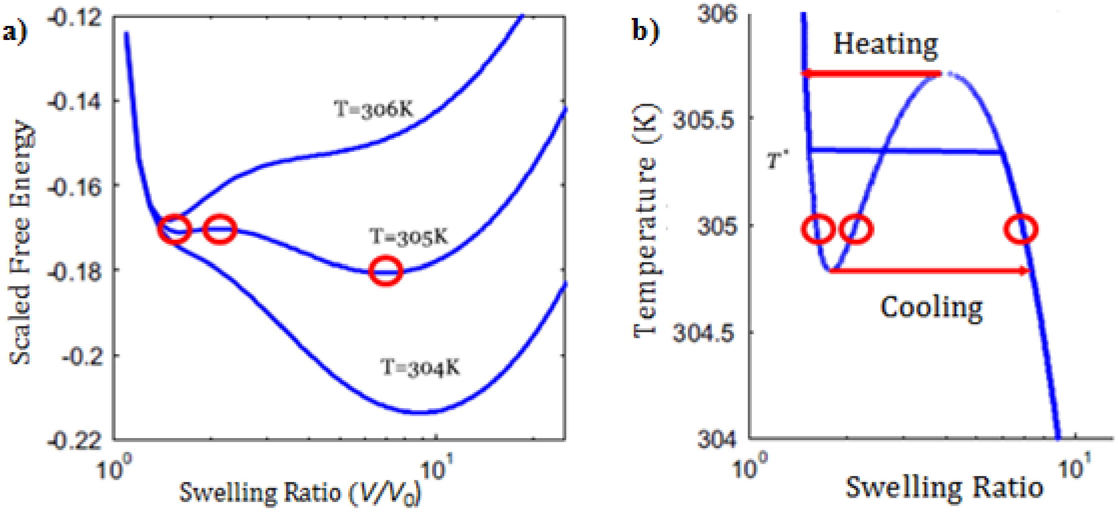

Figure 4: (a) Plotting free-energy for PNIPAM hydrogels reveals the existence of both stable and unstable equilibria (i.e., locations where the first derivative is zero). (b) By collecting these loci of points, heating and cooling pathways can be followed that illustrate the hysteresis effects in swelling and shrinking [21]. T^* indicates LCST.

The previous discussion illustrates the fact that there is some hysteresis in the cooling and heating pathways for PNIPAM hydrogels (Figure 4b). While other studies have reported on this phenomenon [22-24], the effect tends to be glossed over as it is typically negligible. As Figure 4b shows, shrinking occurs at approximately 305.7K while swelling occurs at 304.7K, a difference of only 1K in this example.

In the context of this thermodynamic analysis, the significance of the LCST takes on new meaning; it represents the temperature at which both stable equilibrium points (local minima) possess the same energy. In this light, it should be possible for the gel to spontaneously change state (and volume), provided there is an energetic disturbance to cross the energy barrier separating the two states. Due to the small temperature difference in phase transition on heating and cooling, the LCST is often the only mentioned single phase transition temperature in literature.

1.3 Background on Contact Line Dynamics

In their 1970 publication, Huh and Scriven [25] outlined how describing the motion of a contact line is a deceptively complex process. Whereas most fluid mechanics problems commonly assume a “no-slip” boundary condition for fluid flow past a channel wall, Huh and Scriven argued that imposing such a constraint in fact fails to capture the relevant physics of contact line motion. For a system of two immiscible fluids confined by a solid (e.g., channel), movement of the three-phase contact line means that one fluid must displace the other from the solid surface. In order for this to occur, both fluids must therefore move at some rate relative to the surface during this process. To further this point, Huh and Scriven demonstrated that by applying a creeping flow approximation to the Navier-Stokes equation for contact line motion, a no-slip boundary condition at the channel wall causes shear stresses to approach infinity while approaching the contact line. Given that this phenomenon is clearly unphysical, it is necessary to prescribe some slip condition at the wall [26] in order to correct for this result.

To this day, contact line dynamics are still not fully understood. Due to the difficulty in observing the van der Waals interactions that propel a meniscus forward, what currently exists in literature is a collection of empirical equations that relate contact line velocity to the contact angle [27, 28]. Thus, it is important to recognize that until the problem of a moving contact line can be locally described and understood, there exists a measure of scientific uncertainty in the mechanism of motion that can only be overcome with experimental extrapolations.

1.4 Contact Line Dynamics at Gel Interfaces

Wetting on traditional, “hard” interfaces such as metals is an established research area understood through models and theory proposed by Young-Dupré [29], Wenzel [30], and Cassie-Baxter [31]. Such works traditionally employs free-energy analysis to understand the favorability of a particular wetting state, and thereby enable understanding as to how a droplet may evolve and what equilibrium shape it takes. However, in the case of soft materials such as hydrogels, local deformations near the contact line make the problem more complex. This change of substrate shape can come as a result of: 1) local swelling upon liquid uptake, or 2) viscoelastic deformation induced by the vertical component of the surface tension force acting along the free surface at the contact line of liquid-impermeable soft materials.

In recent years, a series of studies have explored the behavior of sessile droplets on hydrogel films. Intuitively, the phenomenon is similar to the wetting behavior of droplets on elastomers [32, 33] or porous media [34], but made more complex due to the unusual hybrid of liquid/solid characteristics that hydrogels possess.

The next section summarizes very recent work done in this area, discussing results for two general types of gels: swelling and non-swelling. Key findings are discussed in order to establish a context in which to frame and phenomenologically explain the contributions of this work, as introduced in Chapter 2.

1.4.1: Contact Lines Dynamics for Non-Swelling Gels

Several groups have used soft materials in a variety of wetting studies, ranging from evaporating droplets on fiber bundles [35] to contact line evolution for droplets deposited on non-swelling gels [36, 37]. Since these cases involve no mass/volume exchange with the droplets, surface deformations occur strictly due to the vertical component of the surface tension force and have significant effects on contact line dynamics. Such effects can be observed when droplet volume is continuously increased through liquid injection by a syringe pump or other such device.

Kajiya *et al.* [38] studied contact line dynamics for sessile water droplets whose volume increased at constant rates on poly(styrene-butadiene-styrene)(SBS)–paraffin gels. These SBS-paraffin gels were dubbed “hydrophobic” due to the lack of volume exchange between droplet and gel, and were viscoelastic in nature. For high inflation rates (200μL/min), it was found that the contact line spread forward continuously with a constant contact angle. However, at intermediate rates (20μL/min), the contact line displayed a “stick-slip” motion (Figure 5), wherein it underwent a repeated sequence of pinning and sliding. As the contact line remained pinned, the contact angle would increase to a particular value (Figure 5a) before resetting and allowing the contact line to jump forward (Figure 5b). Following this, the value of the contact angle would reset, and the process would repeat (Figure 5c-d). Since no swelling of the hydrogel occurred, local deformation (i.e., ridge formation) on the gel surface must be due to the vertical component surface tension force exerted by the droplet (Figure 5e). On decreasing the injection rate to 2μL/min, it was found that the contact line once again spread in a mostly continuous fashion.

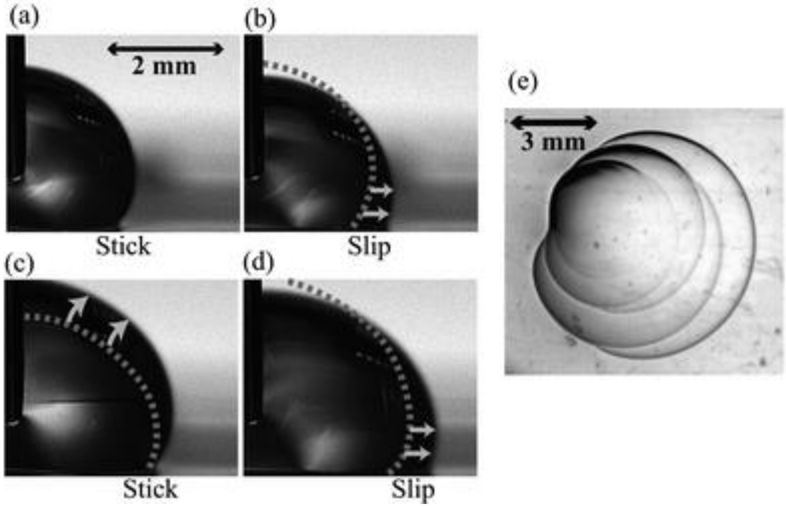

Figure 5: (a-d) Stick-slip behavior for water droplet growth on an SBS-paraffin hydrogel film. The dotted lines in (b-d) indicate the contour of the previous droplet. (e) Overview of the gel surface once the water droplet has been removed. The outlines are deformed ridges resulting from "stick" periods [38].

In order to define three distinct regimes of behavior, the authors defined a characteristic frequency of the contact line motion as:

$$f = \frac{v_a}{R} \qquad 3$$

where f is the inverse of the period over which the contact line moves with velocity v_a for a droplet of radius R. Identifying a cross frequency, f_{cross}, which distinguishes different regimes of behavior, Figure 6 outlines three regimes for droplet motion:

i. $\boldsymbol{f \gg f_{\text{cross}}}$: In this regime, the contact line advances quickly, and the gel in turn responds like an elastic solid. The result of gel deformation is an elastic ridge pull upward by surface tension, propagating forward with the droplet in a continuous fashion.

ii. $\boldsymbol{f \approx f_{\text{cross}}}$: As the contact line velocity decreases, the gel response is no longer purely elastic. Viscous dissipation occurs, and so a part of the surface deformation becomes irreversible. This causes the ridge to act more like a surface defect, pinning the contact line and giving rise to “stick-slip” motion.

iii. $\boldsymbol{f} \ll \boldsymbol{f}_{\mathbf{cross}}$: For the extreme of slow contact line velocities, the gel behaves like a sheet of very viscous fluid with respect to contact line motion. Movement of the contact line drives a capillary flow below the gel surface as the surface tension force shifts forward. This capillary flow drives the surface deformation forward, following the motion of the contact line.

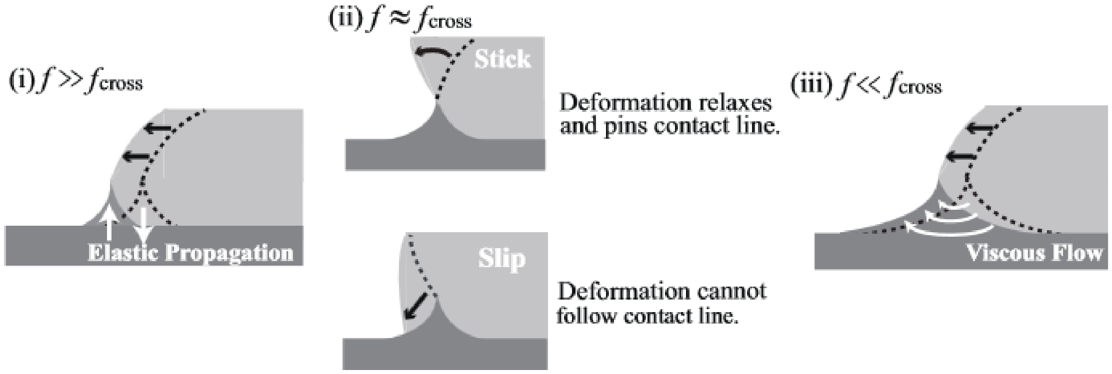

Figure 6: Proposed regime map for contact line advancement over a viscoelastic gel with no volume exchange. [39]

Similar “stick-slip” motion was reported for a variety of liquids (formamide, glyceorl, ethylene glycol, and paraffin oil) on viscoelastic acrylic polymer films [40]. In all cases, the characteristic ridge formation associated with pinning was noted to occur with droplet growth. A complimentary experiment showed that while droplets rolling down an incline coated with monomer 2-ethylhexyl acrylate seemed to exhibit continuous motion, a closer look revealed a series of “stick and break” events related to a repeated sequence of substrate deformation and reestablishment of the contact line [41].

1.4.2: Contact Line Dynamics for Swelling Gels

Wetting of swelling gel surfaces is a phenomenon that has been studied by several research groups, with particular application aimed at understanding how bacteria swarm and migrate [42]. In contrast with the previous section, deformation of the gel surface is now intrinsically tied to liquid permeability, thereby adding another layer of complexity to the problem. The effects of this coupling have only recently been investigated, opening many aspects of the research space that must be explored in order to better characterize the behavior. Banaha *et al*. found that water drops deposited on Agar gels (from the algae extract Agarose) did not spread indefinitely, instead pinning with an angle of 30° until being completely absorbed [43]. Likewise, other studies have examined liquids spreading on hydrogel films, but did not consider the coupling between contact line motion and local deformation due to swelling [44, 45].

Kajiya *et al*. studied the dynamics of depositing water droplets on prepared films of poly(2-acrylamido-2-methyl-propane-sulfonic acid -co- acrylamide (PAMPS–PAAM), a swelling hydrogel [46]. In their work, a 1µL water droplet was placed on a 5mm film of dry hydrogel. In response, water diffused from the droplet into the gel, locally deforming the surface and giving way to the two distinct angles pictured in Figure 7: the contact angle of the droplet relative to the swollen gel surface (θ_{drop}), and the angle of the deformed slope just beyond the contact line (θ_{gel}). After the initial deposition, it was observed that the location of the contact line was pinned as the volume of the droplet decreased due to diffusion into the gel (Figure 8a). As a result, θ_{drop} began decreasing, while the gel continued deforming, leading to an increase in θ_{gel} (Figure 8b). Once $\theta_{\mathrm{drop}} = \theta_{\mathrm{gel}}$, the contact line became unpinned, receding with $\theta_{\mathrm{drop}} = \theta_{\mathrm{gel}}$ until the droplet was completely absorbed. The authors postulated that because the static contact angle on a swollen gel was roughly 0°, the droplet remained pinned until reaching this nearly perfect slip condition.

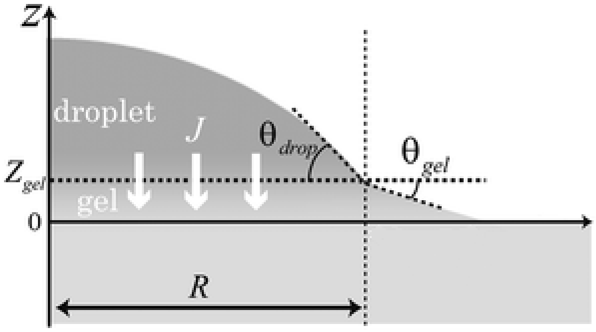

Figure 7: Depiction of a droplet on a swelling hydrogel. As water diffuses into the gel and causes it to deform, two unique angles are formed: θ_{drop}, the droplet contact angle, and θ_{gel}, the angle characterizing the locally deformed slope beyond the pinned contact line [46].

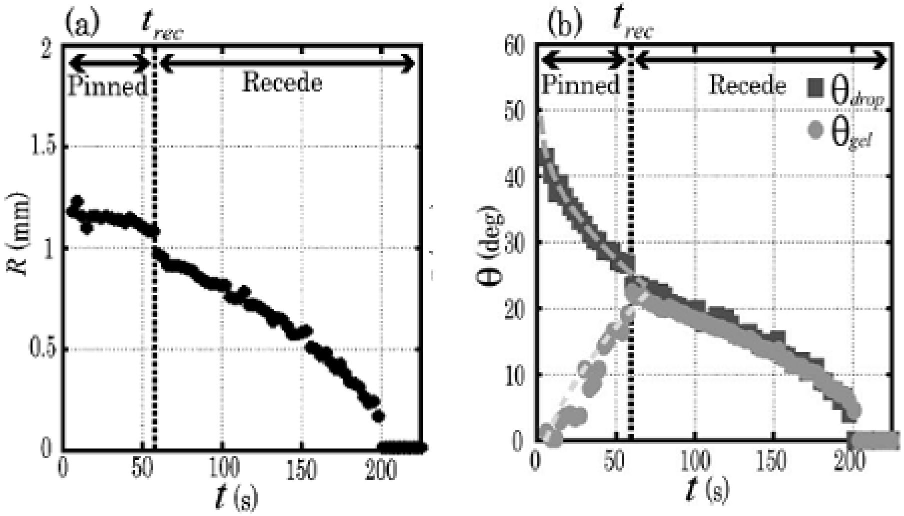

Figure 8: Pinning behavior of a droplet deposited on a dry PAMPS-PAAM hydrogel [46]. (a) The position of the contact line remains pinned until a time t_{rec}, at which it recedes until the droplet is absorbed. (b) t_{rec} corresponds to the time taken for the actual contact angle, $\Delta\theta = \theta_{\text{drop}} - \theta_{\text{gel}}$ to equal 0°, the reported equilibrium value for a droplet on a swollen film.

1.5 Summary

This chapter provided a general introduction to key characteristics of PNIPAM, with a primary focus on the phenomenon of hydrogel wetting. The reviewed works have provided a general outline to frame the core theme at the heart of this thesis: **complex interactions at water/hydrogel interfaces are due to local deformations and drive unusual, unexpected wetting behavior.** To enhance the current state of the art, this thesis explores the effects of confinement, i.e., how introduction of a PNIPAM hydrogel coating onto an inner wall of a glass capillary impacts the bulk flow of water through these capillaries. Chapter 2 begins by detailing synthesis for the polymer coatings, and describes the experimental setup used to track meniscus position for bulk flow of water. Meniscus tracking data is compared for capillary pressure driven flow of water and glycerol (shown not to induce swelling), and results are compared against theoretical predictions taken from Poiseuille flow. Knowledge of contact line pinning introduced in this chapter's literature review is applied and use to help interpret results.

CHAPTER 2

LIQUID BEHAVIOR IN PNIPAM GATED CAPILLARIES

As introduced in Chapter 1, hydrogel wetting is a complex research topic that has only recently been explored for planar geometries. In this work, a hydrogel coating was synthesized along the inner diameter of glass capillaries, driving the focus of this research to be an open exploration of how interactions at the hydrogel/water interface dramatically changes the nature of fluid flow through the PNIPAM gated capillary. This chapter begins by detailing the method for synthesizing PNIPAM layers in capillaries and on planar samples, and then moves on to describe the experimental setup for dual characterization of meniscus position and hydrogel swelling for PNIPAM gated capillaries. Initial results for meniscus position tracking and compared against a well characterized problem (Poiseuille flow) for two different fluids: water and glycerol (which was shown not to initiate swelling of the PNIPAM hydrogel).

2.1 Sample Synthesis

2.1.1 Capillaries Gated with PNIPAM Coating

Borosilicate glass capillaries from Sutter Instruments of two different inner diameters (300µm and 750µm) were purchased from VWR. N,N'-methylenebisacrylamide (MBA, polymer cross-linking agent), ammonium persulfate (APS 99.99+%, initiator), and tetramethylethylenediamine (TEMED, catalyst), were all purchased from Aldrich, while NIPAM (97%) was purchased from Tokyo Chemical Industry. Prior to synthesizing the PNIPAM hydrogel layer, the capillaries were cleaned following a standard lab procedure using piranha solution (Appendix A). Capillaries were then silanized in order to form a bonding agent between the glass and the PNIPAM hydrogel. The method for silanizing samples was taken from a protocol reported in literature [47]. Briefly, the samples were immersed in a 0.6 wt% solution of vinyltrimethoxysilane (VTMS 97%, Aldrich) in toluene. Capillaries were carefully placed in solution such that no bubbles were present inside. The dish containing solution and samples was covered and allowed to sit for 2 hours in ambient lab conditions, after which the samples were removed, thoroughly rinsed, and dried with compressed air.

Following this sample pretreatment, a batch of precursor solution was prepared by adding 0.4745g NIPAM, 0.0830g MBA, and 25µL of TEMED to 10mL of nanopure water (18.2 MΩ-cm resistivity). The solution was vigorously mixed for 10 minutes, and then stored at 5°C. When synthesizing the PNIPAM hydrogel coatings, 1mL of precursor solution was withdrawn and mixed with 1.00mg APS in order to initiate the gelling process. Using a syringe, a droplet of this mixture was introduced to one end of a capillary and allowed to fill the inner volume through capillary action. The capillary was then placed vertically (to allow for uniform surface contact between the capillary inner diameter and curing precursor gel solution) into a furnace set at 75°C and allowed to cure for 12 hours.

Figure 9 shows two different cross-sectional views of a capillary upon removal from the furnace. As seen in Figure 9a, the capillary ends were blocked by a buildup of polymer that forms during the curing process. However, by using a diamond tipped scriber to score the capillary outer surface, a 3mm segment was broken off both ends. Examining the cross-section at these new locations, a coating of hydrogel becomes apparent (Figure 9b). Aside from the polymer buildup at the capillary ends, the coating shown in Figure 9b is representative of the cross-section along the capillary length. Using the diamond tipped scriber, all gated capillary samples were broken into 1cm segments prior to conducting experiments.

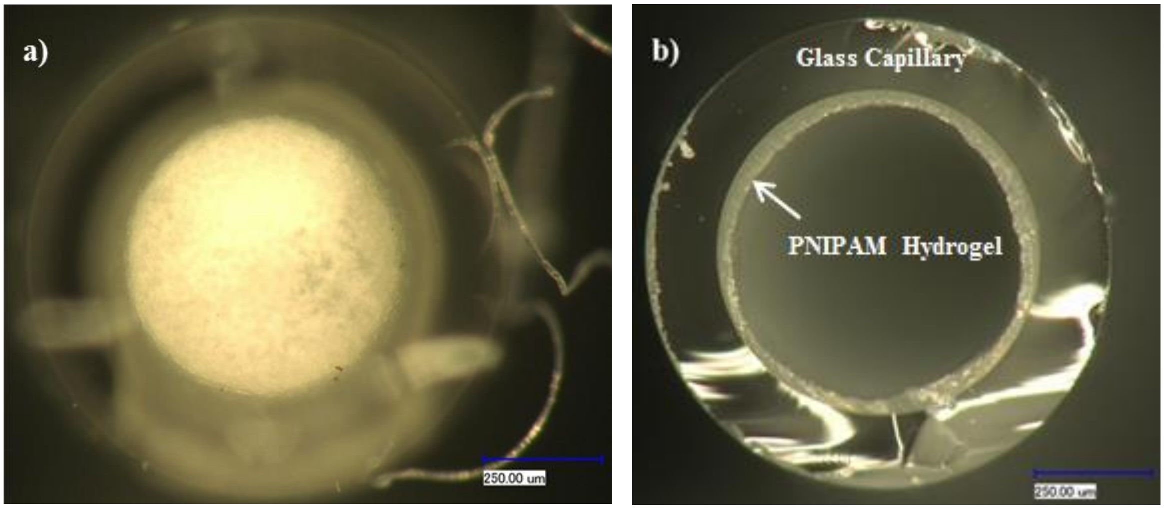

Figure 9: End-on views of the capillary following synthesis of the PNIPAM layer. As pre-cursor solution evaporates during the curing process, there is a buildup of polymer material at the capillary ends (a). However, throughout the rest of the capillary length, a uniform coating of hydrogel has formed (b).

By controlling the concentration of NIPAM in the stock solution, it is possible to control the thickness of the resultant polymer layer. For polymer layers synthesized in 750µm ID capillaries with equivalent amounts of MBA and TEMED, precursor solution with 1.93g NIPAM gives a coating thickness of 42±8µm (Figure 10a), while solution with 0.59g NIPAM gives 13±2µm (Figure 10b). Film thickness measurements were taken for multiple samples, and error is reported with a 95% confidence interval. While thinner coatings (10-20µm) synthesized per this procedure take only 1-2 seconds to reach equilibrium, they do not completely fill the capillary cross-section in their swollen state. Thicker coatings (40-50µm), however, take a longer time to reach equilibrium (~30 seconds), but completely seal the capillary. Thus, hydrogel thickness should be chosen to meet the needs of a target application.

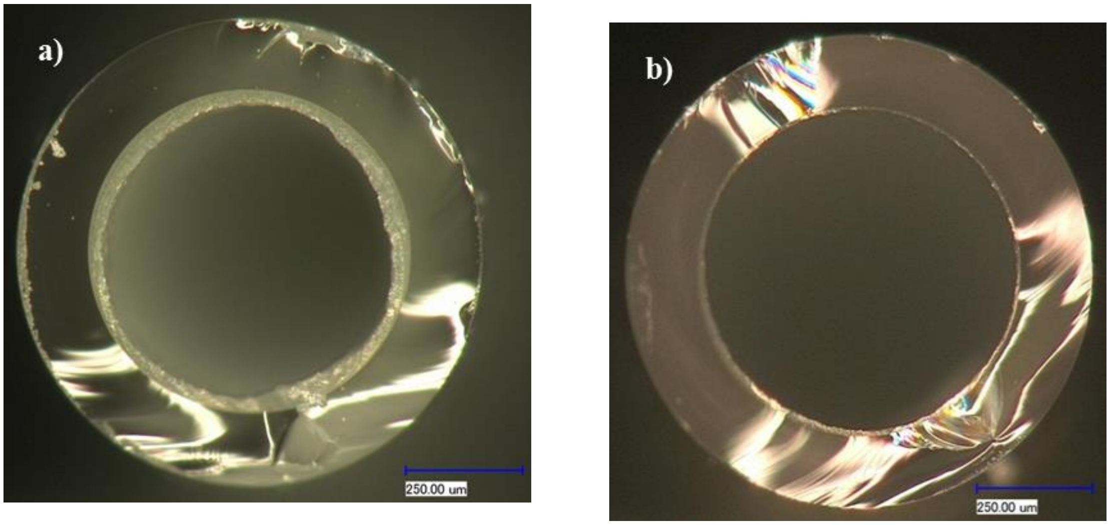

Figure 10: Effect of NIPAM concentration on coating thickness. For equal amounts of crosslinker, catalyst, and water, (a) 1.93g of NIPAM gives a coating with thickness 42±8μm, while (b) 0.59g NIPAM gives a thickness of 11±3μm.

2.1.2 Synthesis of Planar PNIPAM Hydrogels

Due to the opaque color of dried PNIPAM hydrogels, visualization through the gated capillaries was not possible. Therefore, in order to better understand some of the mechanisms governing fluid interaction with the hydrogel, planar samples of comparable thicknesses and chemical compositions were synthesized.

Planar samples were synthesized on silicon wafers, with the procedures for piranha cleaning, silanization, and synthesis of gel precursor solution following the methodology outlined in the previous section. As before, 1mL of precursor solution was withdrawn and mixed with 1mg of APS in order to initiate gel formation. A portion of this mixture was then loaded between a wafer and a glass slide lined with Kapton tape, with the gap distance defining film thickness. The purpose of the Kapton tape was to provide a hydrophobic coating that would discourage the curing polymer from adhering to the cover. A hot plate was used to set temperature to 75°C following deposition of the precursor solution. The planar samples were left covered for 5 minutes, after which the glass slides were removed and the sample was left to cure for 12 hours. Figure 11 shows top and side profiles of the planar samples, with film thickness reported with a 68% confidence interval based on multiple measurements.

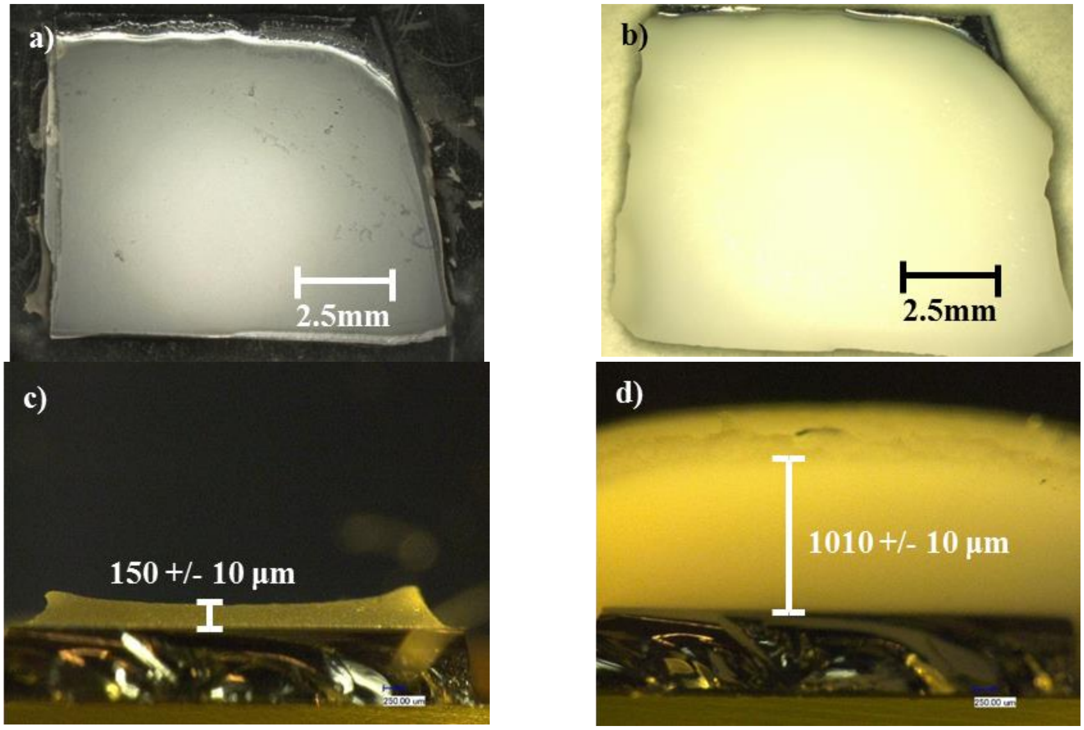

Figure 11: Top and side profiles for dry (a,c) and swollen (b,d) PNIPAM films.

2.2: Experimental Setup

In order to record both contact line motion and swelling behavior, a two camera system was employed (Figure 12). The sample to be studied was placed on a segment of carbon tape and positioned beneath a Keyence Digital Microscope VHX-500F recording at 30fps. Additionally, a MEGAPLUS Redlake ES 1.0 camera was employed to capture end-on view of the sample (i.e., to record swelling). External lighting was adjusted in order to optimize image quality for both cameras.

At the start of each experiment, a sheet of paper was quickly introduced into both fields of view as a means of manually synchronizing the two video streams. Then, a droplet of water was introduced at the back end of the sample (opposite end from which Redlake records data), allowing water to wick through via capillary action. The droplet volume was chosen to be ten times the capillary volume in order to ensure sufficient water for filling the capillary. As the water meniscus traveled through the sample, the Keyence microscope recorded its progress. Upon reaching the opposite end of the capillary, the Redlake camera captured swelling data. A glass slide was placed at this end of the sample so as to prevent distortion from a curved liquid interface.

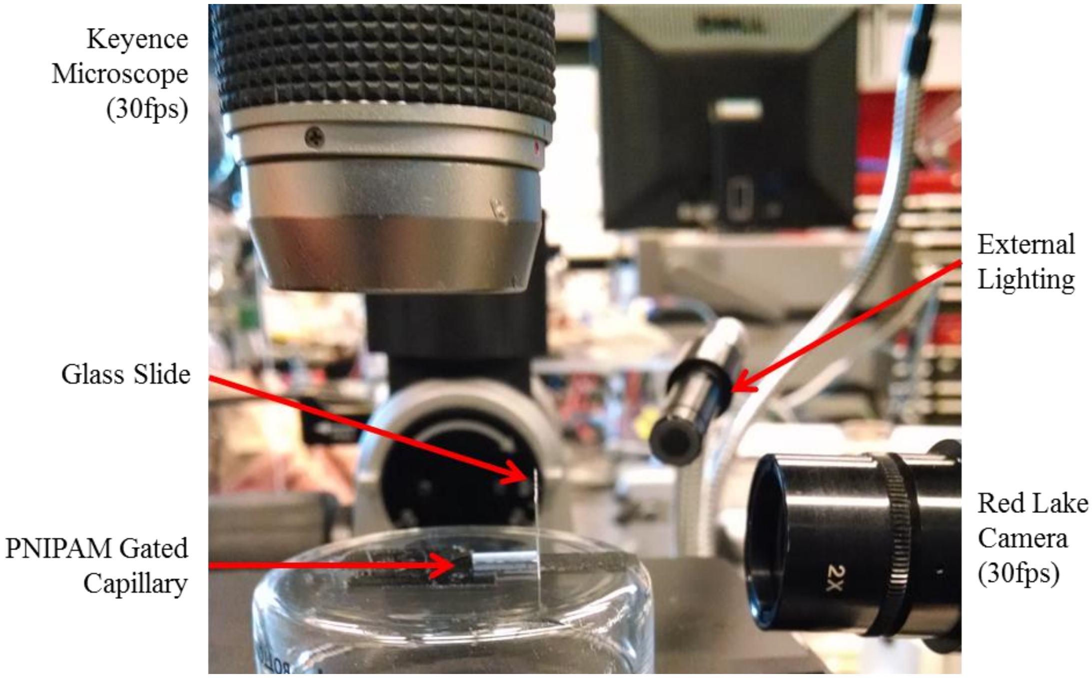

Figure 12: Experimental setup for simultaneously monitoring swelling and contact line motion.

Data for meniscus tracking is introduced in the following section, and forms the primary point of discussion in this thesis. Nonetheless, Figure 13 provides an illustrative example of the data captured by the Redlake camera, demonstrating the swelling process for a hydrogel layer with a dry thickness of 42±8μm. The kinetics of hydrogel swelling have already been extensively studied [48-52]; thus, while swelling data was recorded in each experiment, it served only to supplement observations on meniscus tracking.

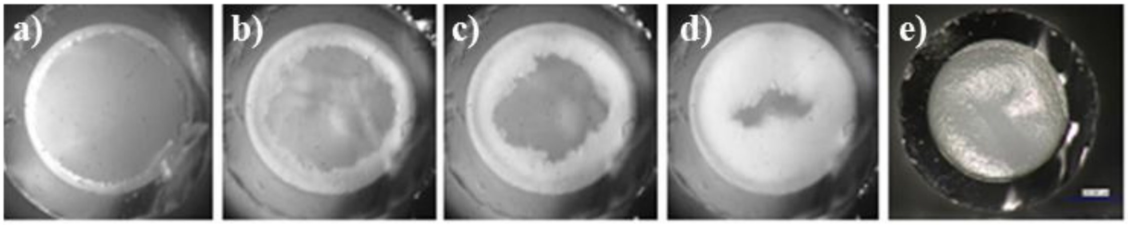

Figure 13: Representative swelling data captured by the Redlake camera for a sample that swells to fill the capillary cross-section.

2.3: Application of Hagen-Poiseuille Equation to Initial Results

The Hagen-Poiseuille Equation [53] follows an Ohm's Law analogy, relating pressure drop (voltage difference) to a volumetric flow rate (current) and characteristic resistance. Employed to model pressure drop across cylindrical pipes, the equation takes the form

$$\Delta P = \frac{128\mu L_{\text{pipe}}\dot{Q}}{\pi d^4} \qquad 4$$

where ΔP is the pressure drop across a pipe of length L and diameter d for a fluid with dynamic viscosity μ and a volumetric flow rate $\dot{Q}$. Equation 4 is derived from the Navier-Stokes Equation under the following set of assumptions:

1. Steady, isothermal flow.
2. Flow is one-dimensional along the length of the pipe.
3. Flow profile is laminar, axisymmetric, and fully-developed.

In the context of the experimental setup described in the previous section, it is desirable to recast Equation 4 into a form that models the position of the meniscus vs. time for flow within a sample. Since droplets are placed at one end of the capillary and allowed to naturally wick in, the pressure difference ΔP is taken as the capillary pressure. For a contact angle θ, a capillary of radius R, and a surface tension value γ this takes the form

$$\Delta P = \frac{2\gamma \cos\theta}{R} \tag{5}$$

Given a constant circular cross-section, the flow rate can be rewritten as

$$\dot{Q} = \pi R^2 \frac{dx_{\mathrm{m}}(t)}{dt} \tag{6}$$

with $x_{\mathrm{m}}(t)$ the position of the meniscus along the sample length. Substituting Equations 5 and 6 into Equation 4 and solving the ordinary differential equation for $x_{\mathrm{m}}(t)$,

$$x_{\mathrm{m}}(t) = \sqrt{\frac{\gamma R t \cos\theta}{2\mu}} \tag{7}$$

In order to validate Equation 7, meniscus tracking was first conducted for bare capillaries (Figure 14). Prior to use, the samples were piranha cleaned. As seen for both the 300μm and 750μm ID capillaries, the meniscus position profiles capture the square root relationship with time. Likewise, since the meniscus position goes with the square root of radius, the 300μm ID capillaries take longer to reach a given length as compared to the 750μm ID capillaries. Regarding the discrepancy between experimental results and the Poiseuille prediction, the theoretical prediction is expected to over predict based on the manner in which the contact angle was determined. Due to the fast movement of the meniscus and the camera limitation of 30 frames per second, a dynamic contact angle could not be visualized. Instead, a static contact angle of 45° was measured by only partially filling a capillary and recording the resultant contact angle. Since advancing contact angles are greater than static ones [54], making this adjustment would bring the theoretical prediction closer to the measured values. Entrance effects are also visible in the experimental data, as the first few points of both inner diameters do not match the steep predicted slope. However, this effect was anticipated, as Equation 7 assumes fully developed flow. Along the hydrodynamic entrance length, the fluid experiences a high shear rate due to the presence of the developing boundary layer, causing the experimental data to undershoot the predicted values. Estimating inlet velocity from Figure 14, Reynolds numbers were calculated to be approximately 36 for the 300µm ID capillaries and 203 for the 750µm ID capillaries. Thus, applying Equation 8 [55], which gives the entrance length, l_e, for laminar flow:

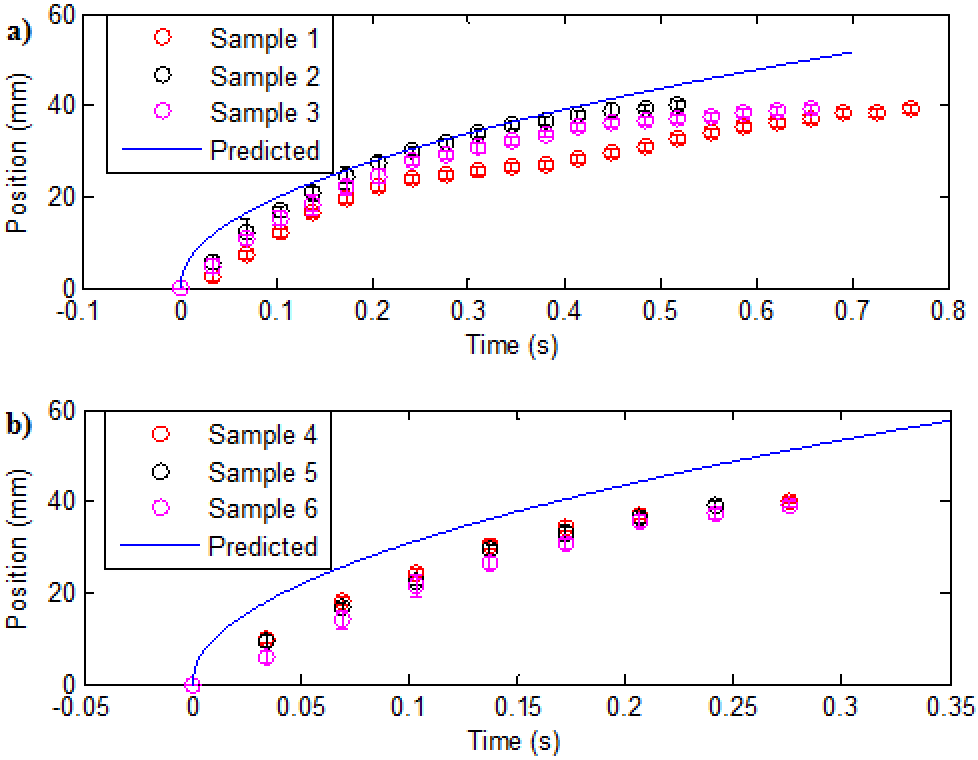

Figure 14: Meniscus position data vs. prediction (θ = 45°) from Equation 7 for (a) 300µm and (b) 750µm ID bare capillaries.

$$l_e = 0.06\ \mathrm{Re} \times d \qquad 8$$

l_e = 6.5mm for the 300 µm ID (Figure 14a) and 9.1mm for the 750µm ID.

Applying Equation 7 to the case of a capillary lined with PNIPAM is non-trivial since the polymer swelling makes the radius, R, a function of both time and space. However, by considering two extremes in swelling timescales, limiting behavior for flow in the PNIPAM gated capillaries can be identified. Figure 15 illustrates two scenarios where the sample radius can be taken as constant: slow swelling, in which the time to fill the capillary is significantly faster than the swelling timescale (Figure 15a), and fast swelling, in which the polymer swells to its equilibrium shape as soon as the meniscus moves forward (Figure 15b).

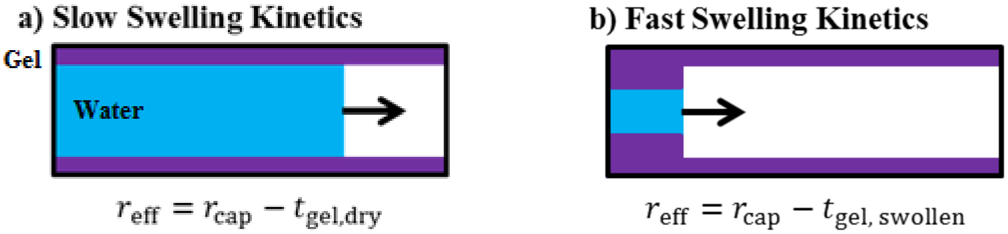

Figure 15: Limiting cases for modeling capillary flow through a capillary lined with a PNIPAM coating.

Figure 16 presents data for meniscus tracking with various samples gated with PNIPAM. The “G” in the legend refers to “gated,” while the sample numbers correspond to those in used Figure 14. Thus, Sample 1G is the same capillary used in the bare capillary experiments (Figure 14, Sample 1), but with an added layer of polymer. Table 1 provides additional data for the sample properties, including the dry and swollen thicknesses for the hydrogel layers; error bars reflect 68% confident intervals based on multiple measurements of dry/swollen thickness. As apparent in Figure 16a, the experimental data lays nowhere close to the upper and lower limiting case Poiseuille predictions defined in Figure 15. In fact, by examining the experimental data on a more appropriate scale, it becomes clear that the time to wick along the gated capillary length undershoots prediction by two orders of magnitude. Comparing the time for wicking through a 10mm section of gated capillary to the time for wicking through a 10mm section of bare capillary, the difference is roughly 90 seconds vs 0.05 seconds. These results are completely unexpected: *coating a hydrophilic material (glass) with a gel that is hydrophilic at room temperature results in a filling time that is 1000 times longer.*

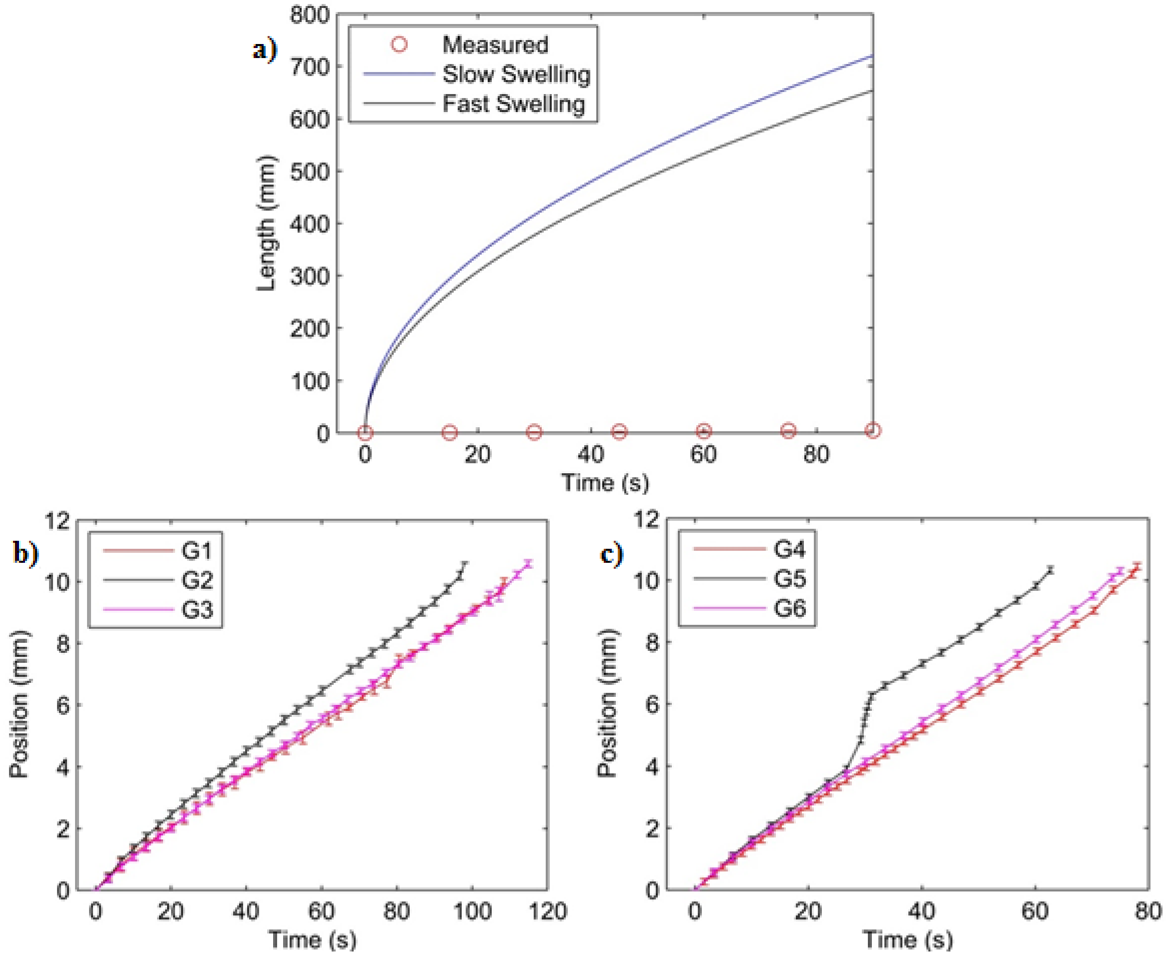

Figure 16: Data for meniscus position vs. time in PNIPAM gated samples. (a) Comparing experimental data to limiting cases of Equation 7 ($\theta = 60°$). (b) Profile for 300μm ID and (c) 750 μm ID capillaries. Note that in (b) and (c), line segments connecting data are only meant to aid visualization of the linear profile. Error bars represent measurement uncertainty per data point.

Table 1: Sample Data for G1-G6 in Figure 16

Sample Number	Capillary ID (μm)	Gel Dry Thickness (μm)	Gel Swollen Thickness (μm)
G1	300	8 ± 0.5	19 ± 1
G2	300	8 ± 0.4	28 ± 2
G3	300	8 ± 0.7	23 ± 1
G4	750	12 ± 2	63 ± 7
G5	750	14 ± 2	53 ± 6
G6	750	12 ± 2	53 ± 7

In using Equation 7 to show predicted values in Figure 16, there was some ambiguity as to what value should be used for the contact angle. A value of $\theta = 60°$ was chosen, based on very conservative estimates in literature for water droplets on swollen PNIPAM films [56, 57]. Nonetheless, it was recognized that there existed some ambiguity in choice of contact angle in light of the fact that PNIPAM's opaque color prevented visualization through the capillary of contact line dynamics. Thus, since all other parameters in Equation 7 were well characterized, an artificial value of θ was chosen in order to produce a theoretical prediction on the same order of magnitude as the experimental data. Using data from sample G2 in Figure 16, Figure 17 shows that a virtually 90° contact angle is required. Furthermore, the profile of the prediction fails to match the experimental data's linear behavior. Considering these observations, it was concluded that the capillary driven flow through the PNIPAM gated samples did not merely result in a change of radius or contact angle. Instead, it was hypothesized that complex interactions occurring at the hydrogel/water interface were responsible for the large change in behavior.

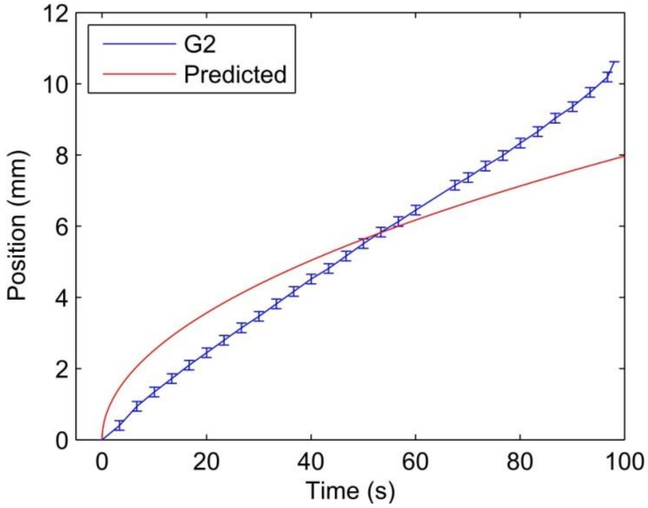

Figure 17: Setting θ = 89.985° in Equation 7 gives a prediction that is of the same order of magnitude as the experimental data, but fails to capture the linear profile.

2.4 Meniscus Tracking for Glycerol in PNIPAM Gated Capillaries

Capillary filling of PNIPAM gated capillaries was repeated using glycerol (99.99%) instead of water. A primary motivation for using glycerol was that it was shown not to interact with the PNIPAM hydrogel (Figure 18), hence removing the complicated interfacial phenomena introduced by swelling and hydration. Additionally, glycerol's surface tension (64mN/m) is similar to that of water (72mN/m), thereby providing a measure of hydrogel deformation due to surface tension forces.

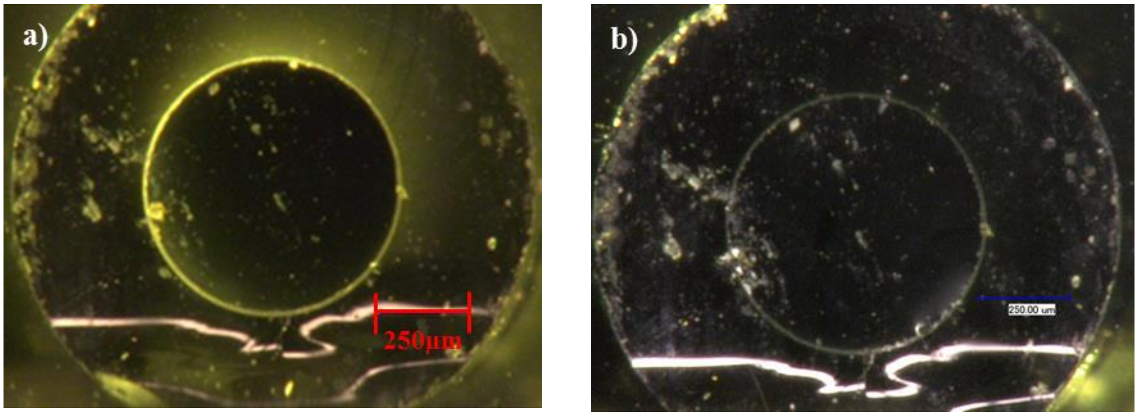

Figure 18: Gated capillary with thin coating of PNIPAM (a) before and (b) after filling with glycerol.

In order to quantify the contact angle in Equation 7, rough contact angle measurements were conducted for several glycerol droplets deposited on planar PNIPAM films of comparable thickness and composition (i.e., same NIPAM and crosslinker wt%) to the gated capillaries. These measurements used basic software from ImageJ (distributed by NIH) to fit curves to images of droplet profiles in order to calculate contact angles. This gave measurements of 80±6° based on the maximum/minimum values for this non-rigorous technique.

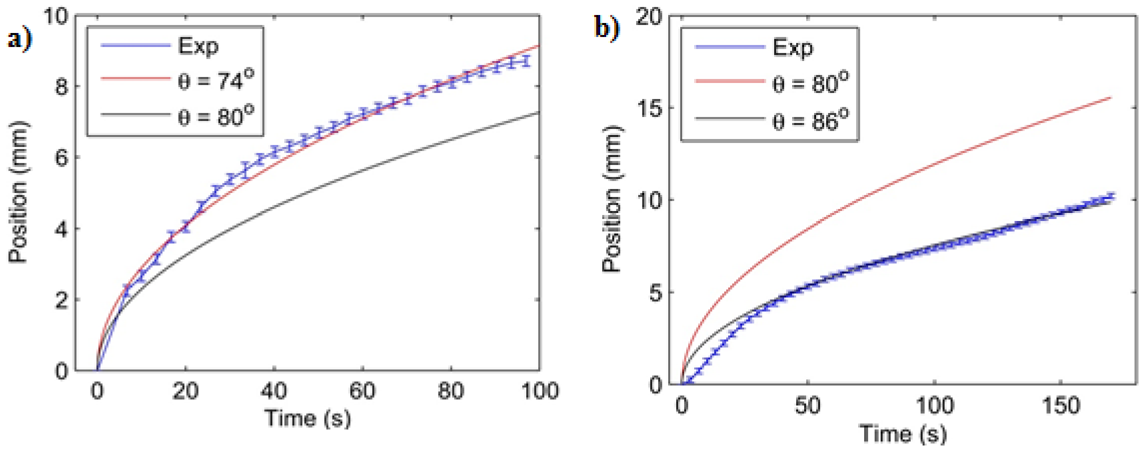

Figure 19: Meniscus position vs. time for glycerol in (a) 300μm and (b) 750μm ID capillaries lined with PNIPAM layers.

As seen in Figure 19, the measured profile of meniscus position vs. time does a good job of following experimental predictions within the error associated with the contact angle measurement. For both size capillaries (300μm and 750μm ID), the square root relation with time is apparent. Since glycerol was shown not to induce swelling in the PNIPAM hydrogels, these results are important in that they help to establish a baseline by removing the interaction between gel and fluid. This, in turn, strengthens the hypothesis that complex interactions due to swelling/interface dynamics are responsible for the water behavior in Figure 16a.

2.5 Summary

This chapter began by outlining two different techniques for synthesizing PNIPAM films and gated capillaries. Piranha cleaning activated glass/silicon surfaces, while silanization allowed for a bridge to create bonds between the gel and substrate. These processes are straightforward, requiring supplies found in a typical lab and eliminating the need for specialized setups.

By integrating two synchronized cameras into the experimental setup, swelling data and meniscus tracking could be simultaneously captured to provide a link between the two phenomena. From this data, it was shown that introducing a thin 10-20μm layer of PNIPAM hydrogel had a dramatic effect on the motion of a meniscus driven by capillary pressure. Comparing meniscus position data of PNIPAM gated capillaries vs. bare capillaries, water was shown to take 1000 times longer to propagate through a 1cm length capillary. This surprising result fell far below Poiseuille predictions, even when adjusted for different extremes of swelling dynamics.

In order to establish a baseline, meniscus tracking experiments were conducted utilizing glycerol as the working fluid. Swelling visualization of PNIPAM lined capillaries showed that glycerol does not initiate swelling of the hydrogel, and profiles for meniscus position were shown to be in good agreement with Poiseuille predictions. These results helped strengthen the hypothesis that complex interactions at the PNIPAM/water interface were responsible for the dramatic change in behavior.

Chapter 3 builds on these results, by exploring how dry gel leads to contact line pinning. Forced flow experiments are used to validate that gated PNIPAM capillaries follow Poiseuille predictions for their characteristic pipe. Additionally, the effects of different drying techniques are explored in order to postulate how the presence of entrained water can reduce pinning. Likewise, gated capillaries are prepared with both swollen and dry segments to show how the effect of pinning is much more exaggerated for dry polymer. Finally, a theoretical framework is adapted from literature in order to model the sequence of events that result in pinning/unpinning events. Scaling analysis allows for an estimation of time total for water through the gated capillary, and allows for comparison with experimental data.

CHAPTER 3

ANALYSIS OF CONTACT LINE PINNING IN PNIPAM GATED CAPILLARIES

In Chapter 2, it was shown that introducing a thin layer of PNIPAM hydrogel to glass capillaries has a dramatic effect on water flow. Through a series of experiments, the following observations were made:

- Experimental data for flow through a capillary lined with PNIPAM reveals that the time for water to travel the 1cm length is three orders of magnitude less than corresponding Poiseuille predictions.
- A contact angle of virtually 90° is necessary in order to bring Poiseuille predictions to the same order of magnitude of experimental data for water. Yet, PNIPAM is hydrophilic at room temperature.
- Experimental data shows a linear relationship between distance traveled by the water meniscus and time, while Poiseuille theory (Equation 7 predicts a square root relationship with time.
- Pure glycerol, which was shown not to induce swelling, does follow Poiseuille predictions in PNIPAM gated capillaries.

Together, these results support the hypothesis that swelling at the gel interface leads to complex contact line dynamics. Additionally, this hypothesis was strengthened by the results presented in Figure 20, which show plots of water meniscus position vs. time under high magnification (200x). In-house edge detection software was written in order to examine contact line behavior for small segments of the PNIPAM gated capillary (700µm in length vs. the total 1cm length) at small time steps (0.03s, the limit of a 30fps camera). In doing so, a series of "stick-and-slip" events manifest themselves, particularly in the case of the 750µm ID channels (a-b). Though not as evident in the 300µm ID channels (c-d), this may be due to the fact that the events occur on smaller timescales and over smaller distances (see Section 3.4.2). Nonetheless, the data does demonstrate a repeated sequence of pinning/unpinning events, which this chapter will analyze and interpret.

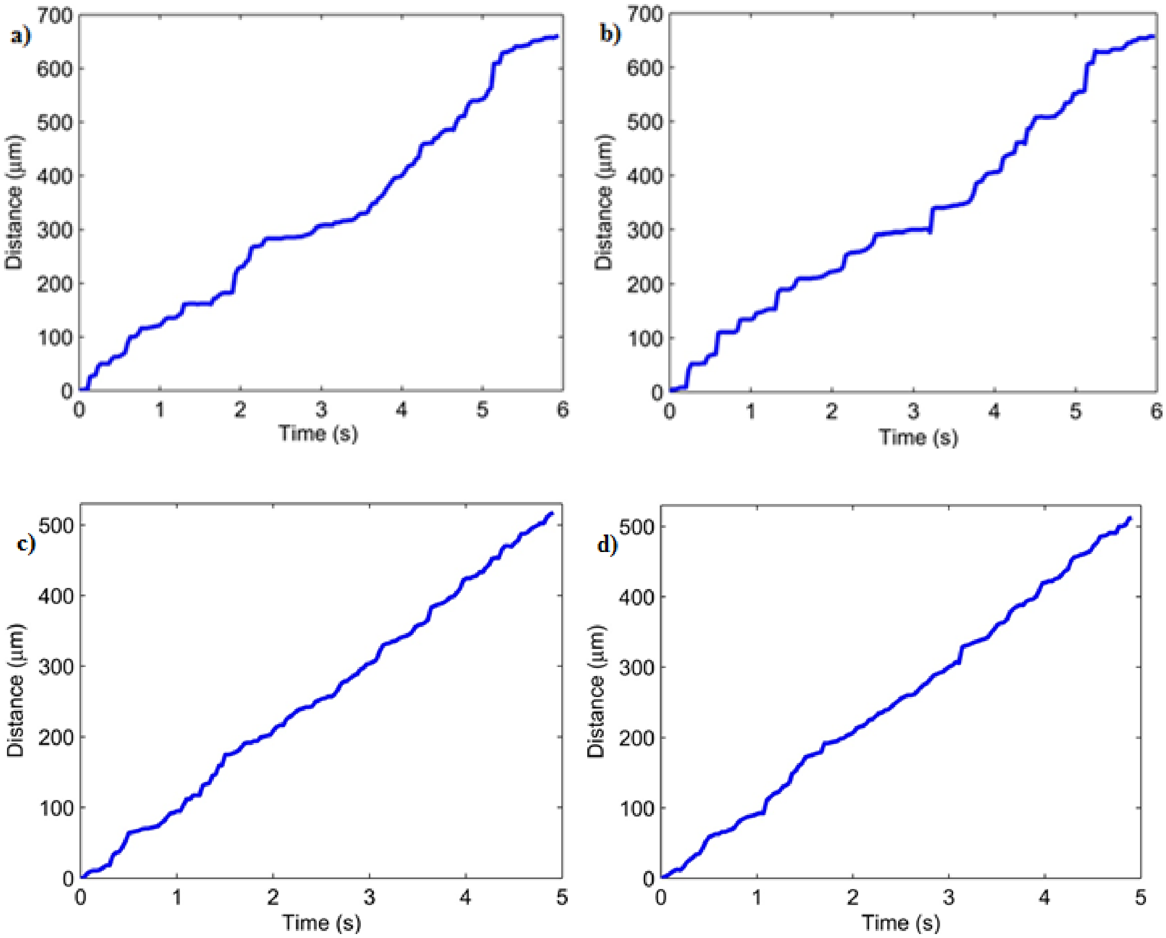

Figure 20: Meniscus profile at 200x magnification for (a-b) 750µm ID and (c-d) 300µm ID gated capillaries. Error bars (±8µm) reflect instrumentation error and are not pictured in order to improve readability of the plots.

Thus, the discussion of this chapter builds on this idea by first examining forced flow experiments to demonstrate that the fully swollen polymer can essentially be treated as an additional layer of glass, merely acting to decrease the effective capillary diameter. It continues by examining the ways in which drying gated samples affects contact line pinning. The effect of residual water on contact line pinning is discussed, and tied in with results that show sharp transitions in meniscus velocity for capillary pressure driven flow in samples with segments of both dry and swollen polymer. Finally, a theoretical framework is proposed to define the physical mechanism of contact line pinning, showing how the evolution of the meniscus contact angle and the swelling gel interface together give rise to the observed "stick-slip" behavior. Scaling analysis is employed to complement this framework, offering some insight into the fluid transport and providing estimates for time of water penetration through the gated samples, which is compared to experimental data.

3.1 Forced Flow Experiments with PNIPAM Gated Capillaries

In comparing experimental data to Poiseuille-based predictions, it was implicitly assumed that the characteristic resistance for a capillary gated with PNIPAM follows the form assumed for a smooth pipe:

$$\text{Flow Resistance} = \frac{\pi d^4}{128 \mu L_{\text{pipe}}} \qquad 9$$

where d is the effective diameter, μ is the dynamic viscosity of the working fluid, and L_{pipe} is the pipe length. In order to validate this assumption, pressure drop was measured across capillaries with swollen PNIPAM hydrogels. As a baseline experiment, pressure drops were measured across bare capillaries and compared to Poiseuille predictions in order to validate application of the theory.

3.1.1 Experimental Setup and Results for Bare Capillaries

Figure 21 illustrates the experimental setup used for measuring pressure drop in forced flow experiments. Pressure was measured with a LabSmith uPS0800-T116 transducer, and capillary tubing/sleeves/fittings were purchased from Upchurch Scientific in order to connect the microfluidic assembly. The chosen syringe had a volume of 50mL and an inner diameter of 27.45mm, allowing for flow rates between 0.2 and 500mL/hr to be set on a KD Scientific Model 100 syringe pump. As indicated in Figure 21, the position of pressure transducer is not right at the inlet of the capillary, meaning that it measures a total pressure drop across the 4.3cm length of PEEK tubing, the adapter, and the capillary. However, a short length of PEEK tubing with a large inner diameter (750μm) was chosen in order to minimize the pressure drop along this section, while the pressure drop across the adapter was likewise shown to be negligible. In experiments, the capillary outlet was exposed to open atmosphere. Thus, by taking pressure at the capillary outlet to be atmospheric and zeroing the transducer to this value, the measurements read by the transducer were taken to be a fairly accurate representation of the pressure drop along the capillary sample.

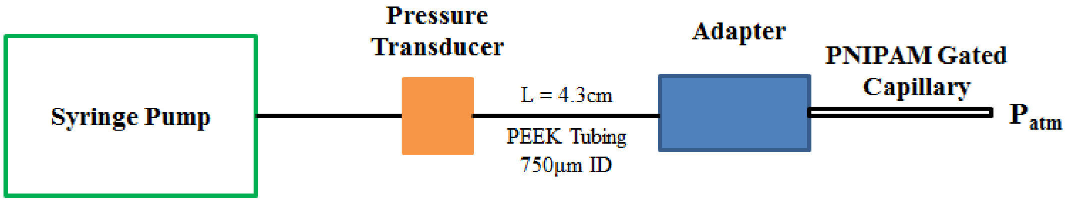

Figure 21: Experimental setup for measuring pressure drop along PNIPAM gated capillaries.

Figure 22 shows pressure drop for a bare 300μm ID capillary of varying length. The capillary was scored with a diamond-tipped scriber in order to be broken to a given length. As can be seen, the data points follow a linear trend (as predicted by the Poiseuille relationship between pipe length and pressure drop) and are in general agreement with the theoretical predictions from Equation 4. Due to the presence of bubbles trapped in the microfluidic setup, pressure measurements were seen to fluctuate about a mean value, thereby giving way to the error bars reported in Figure 22.

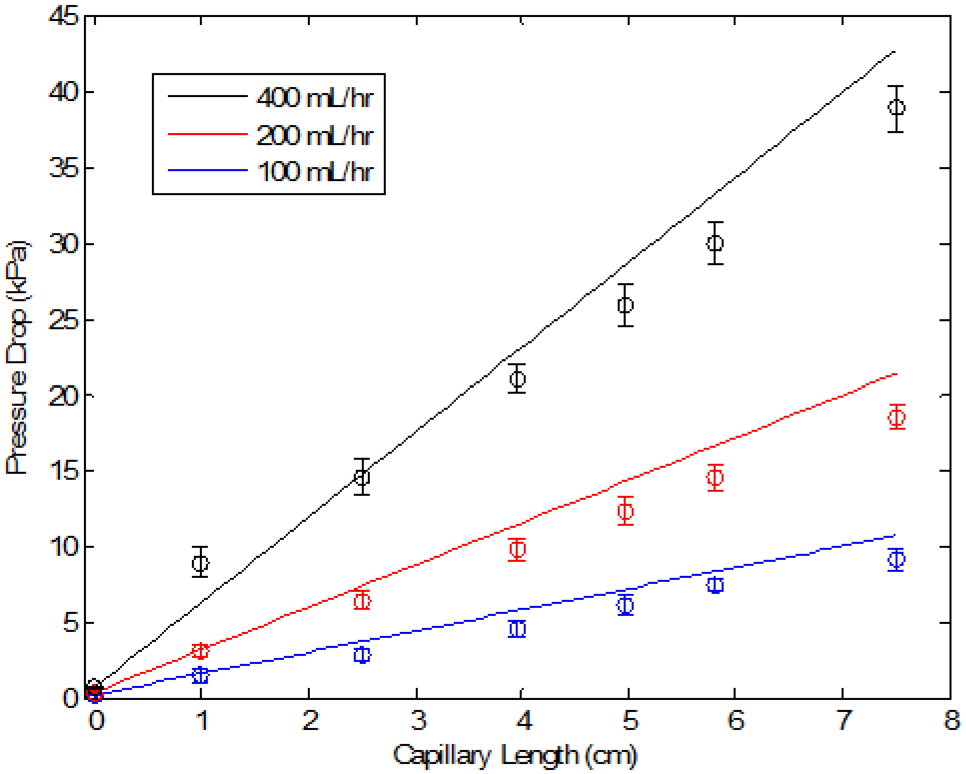

Figure 22: Pressure drop measurements for bare capillary (ID=300μm) cut to varying lengths. Lines indicate predictions based on Poiseuille theory while circles are experimental values.

One point that has gone unmentioned is the effect of surface roughness, as Poiseuille flow assumes a smooth surface. As the data in Figure 22 indicates, this is a fair assumption for bare capillaries, but may not necessarily be true for PNIPAM coatings due to non-uniformity in the ring thickness. Furthermore, deviations between theoretical predictions and experimental data cab largely be accounted for by the sensitivity of Equation 7 to the value of the capillary inner diameter. Given the variability of ΔP with diameter to the fourth power, small variations in the diameter likely account for the difference between experiment and theory. More importantly, the fourth power relationship drives the need for particularly precise diameter measurements in order to produce results with reasonable error.

3.1.2 PNIPAM Gated Capillaries

After validating Poiseuille pressure drop predictions with experimental data for bare capillaries, a PNIPAM gated capillary was swapped into the setup depicted in Figure 21. Due to the fast kinetics of the thin PNIPAM gels (1-2s to swell to equilibrium) and a minimum time step of 0.5s between pressure readings, it was not possible to generate accurate pressure profiles during the period of hydrogel swelling. Thus, pressure drop data was collected for capillaries with swollen hydrogel layers.

Figure 23 compares pressure drop measurements for a 300μm ID bare capillary and a 300μm ID capillary with a 17μm thick layer of swollen hydrogel. As noted previously, the oscillations in the pressure profile are likely due to bubbles present in the microfluidic setup. In both cases, the pressure drop is higher for the gated capillary as a result of the smaller effective diameter.

The results of these forced flow experiments are summarized in Table 2 and Table 3. The entrance length is calculated following Equation 8, while the Reynolds number is calculated as

$$\mathrm{Re} = \frac{\dot{Q} d_{\mathrm{eff}}}{\vartheta A} \qquad 10$$

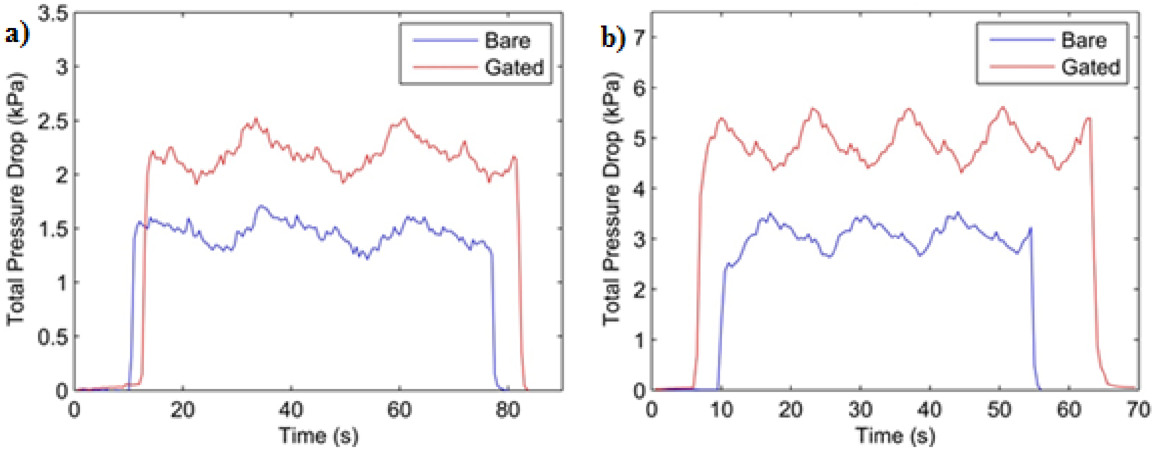

Figure 23: Comparison of pressure profiles for a bare and gated capillary sample for flow rates of (a) 100mL/hr and (b) 200 mL/hr.

where $\dot{Q}$ is the volumetric flow rate, ϑ is the kinematic viscosity, A is the cross-sectional area, and d_{eff} is the effective diameter (equal to capillary ID minus twice the gel thickness for the PNIPAM gated sample). Upon completion of the experiment, the thickness of the PNIPAM coating in the gated capillary was measured to be 17±3μm, with the error reflecting a 95% confidence interval based on multiple measurements. This gave an effective inner diameter of 266μm for calculating the Poiseuille prediction pressure drop across the gated sample with swollen polymer. For both the bare and gated capillaries, experimental data shows very good agreement with the predicted values at 100 and 200mL/hr. Although the measured values overshoot the predicted values at 400mL/hr, this is expected given that the hydrodynamic entry length (approximately 8.5mm in both cases) accounts for most of the sample length (1cm). Since the Poiseuille equation assumes full-developed flow, it does not account for the increased pressure drop due to flow acceleration and increased shear wall stress in the boundary layer. Thus, from these results, it is concluded that the pipe resistance for a PNIPAM hydrogel can be modeled by Equation 9. This leads to the conclusion that water penetration into PNIPAM gated capillaries is in fact driven by capillary pressure (as opposed to some other mechanism), but face repeated pinning due to the presence of dried hydrogel.

Table 2: Experimental Data vs. Poiseuille Predictions for 300μm ID Bare Capillary

Flow Rate (mL/hr)	Reynolds Number	Hydraulic Entry Length (mm)	ΔP Predicted (kPa)	ΔP Measured (kPa)
100mL/hr	117	2.1	1.4	1.5 ± 0.2
200mL/hr	235	4.2	2.8	3.0 ± 0.3
400mL/hr	470	8.5	5.6	9.0 ± 0.5

Table 3: Experimental Data vs. Poiseuille Predictions for 300μm ID Gated Capillary

Flow Rate (mL/hr)	Reynolds Number	Hydraulic Entry Length (mm)	ΔP Predicted (kPa)	ΔP Measured (kPa)
100mL/hr	133	2.1	2.3	2.3 ± 0.3
200mL/hr	267	4.2	4.6	4.6 ± 0.4
400mL/hr	532	8.5	9.2	12.3 ± 0.8

3.2 Qualitative Observations the Effect of Dehydration

After performing any flow experiments involving hydration of PNIPAM gated capillaries, it is necessary to return the hydrogel to its dry, baseline state before conducting further experiments. However, over the course of this work, it was found that the way in which this sample "rejuvenation" is performed has important consequences on the measured meniscus position in subsequent experiments. This can be seen in Figure

24, which shows four sequential runs of a 750µm ID capillary with a 12µm layer of dry PNIPAM. Figure 24a shows meniscus tracking for the first experimental run immediately following synthesis of the hydrogel layer, and is characterized by a time of nearly 80s for water to penetrate through the 1cm length of the capillary. In between the subsequent runs (b-d), the sample was stored in a vacuum furnace at 40°C (above the polymer LCST) and -0.08MPa (relative to ambient pressure) for three hours. The time for water to penetrate through the sample falls will subsequent runs, from 80s to 12s in (b), and to approximately 0.45s in (c) and (d).

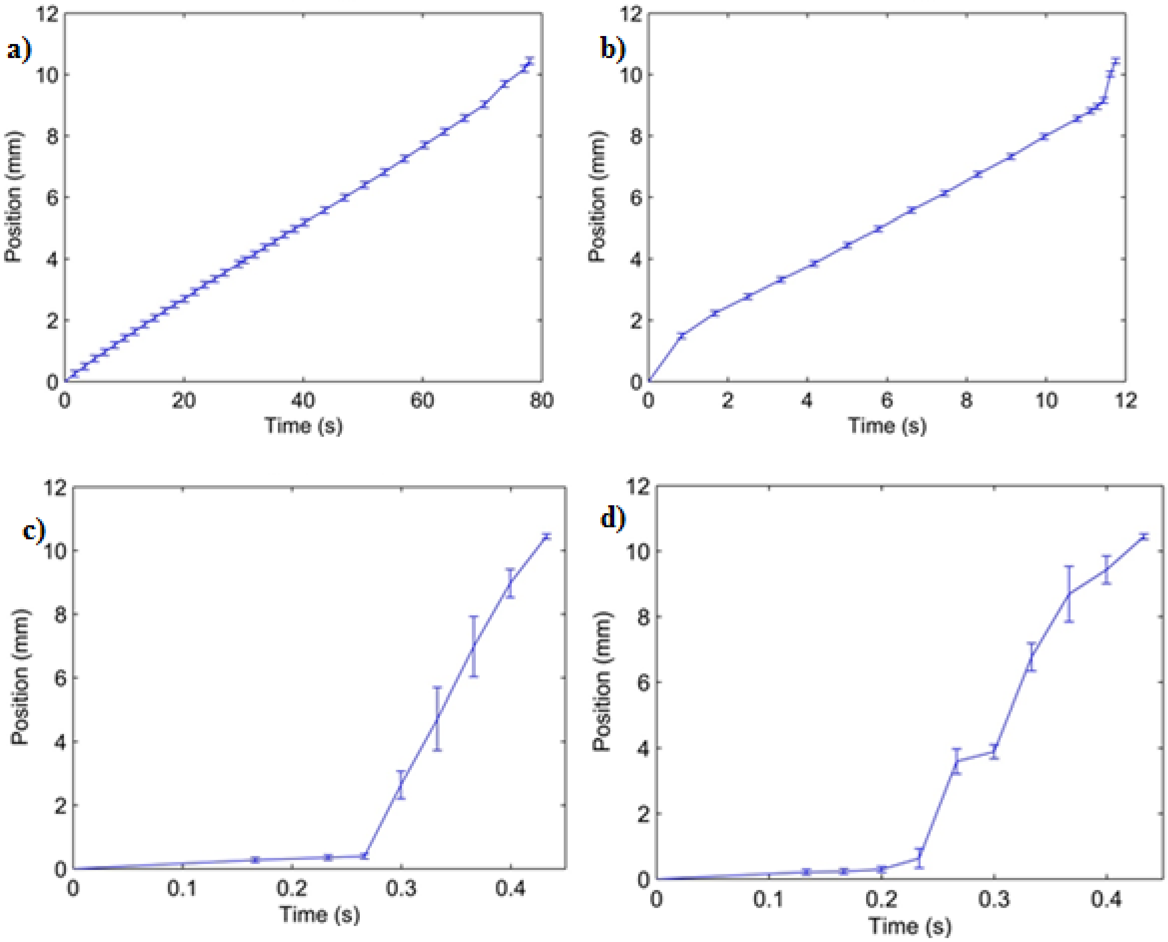

Figure 24: Four sequential meniscus tracking experiments. Data in (a) comes from a run immediately following sample synthesis, while rejuvenation conditions in subsequent runs (b-d) are 40°C and -0.08MPa for 3 hours.

This dramatic drop in the time to travel the capillary length can be explained by the fairly mild conditions at which the sample was stored. Although 40°C is above LCST, and prompts phase separation of water from the hydrogel, it is still below 61°C, boiling point of water at the vacuum furnace pressure (20kPa). Furthermore, the geometry of the capillary limits mass transfer of water (and hence, evaporation). For these reasons, it is therefore likely that under these mild conditions, residual water remains adsorbed on the gel surface. Once the gated capillary is removed from the vacuum furnace and begins to cool below LCST, the water is absorbed locally into the gel surface. As Section 3.3 discusses, the contact line experiences significantly more pinning when in contact with dry gel than with swollen gel, explaining why the time for water to penetrate through the capillary decreases from the value set for experiments just after curing.

This phenomenon can also be observed for samples rejuvenated for the same period of time at different temperatures. A sample kept at 75°C for 18 hours between experiments (Figure 25, a-b) shows consistent meniscus tracking data between runs. However, the time to penetrate through the gated capillary significantly varies from a sample kept at 110°C for the same amount of time (Figure 25, c-d). Thus, the main takeaway here is that conditions chosen for dehydrating a sample in between runs have strong impacts on the observed meniscus velocity as entrained water helps to reduce the effects of pinning from the hydrogel. This is important to bear in mind, as the extent of hydrogel dehydration could impact performance in a target application.

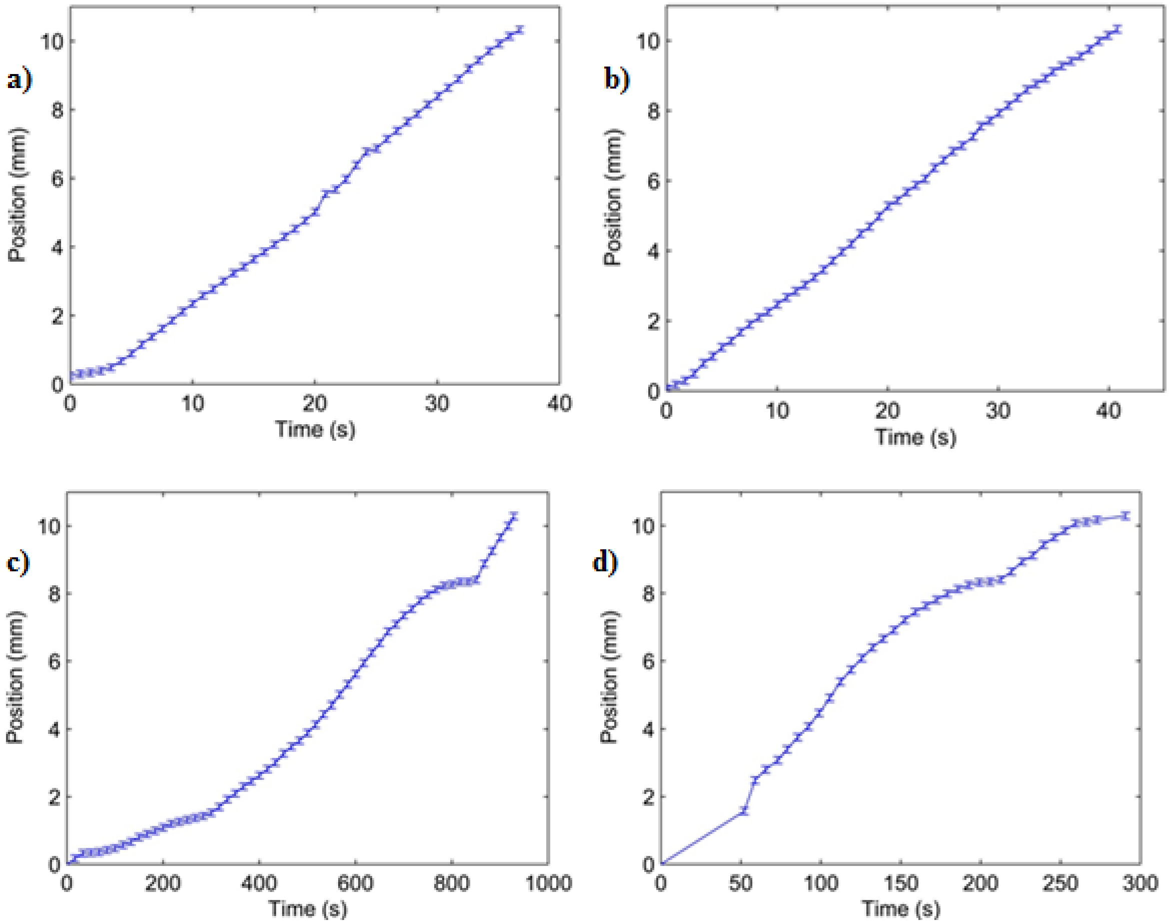

Figure 25: Meniscus tracking for (a-b) a 750µm ID gated capillary rejuvenated at 75°C for 18 hours and (c-d) a second 750µm ID gated capillary rejuvenated at 110°C for 18 hours.

3.3 Samples with a Combination of Swollen and Dry Segments

In order to explore the hypothesis that regions of dry polymer pin the contact line, samples were treated in order to contain both dry and swollen segments. To do so, glass capillaries with dry PNIPAM layers were placed in DI water (room temperature, below LCST) and allowed to soak for 3 hours in order to reach an equilibrium swollen state. As noted in Table 1 of Chapter 2, these PNIPAM layers had dry thicknesses from 10-20µm, and swollen thicknesses of 20-60µm. The samples were then removed, and a light stream of compressed air was introduced at one end of each sample in order to force out bulk water that had not diffused into the polymer. Next, the samples were left in ambient lab conditions in order to allow water in the hydrogel to begin evaporating. This produced a sample with a region of dry polymer near the capillary ends and a region of swollen hydrogel throughout the remainder of the capillary. As indicated by Figure 26, these regions were distinguished by distinct changes in color from opaque (dry hydrogel) on both ends, to white (swollen hydrogel).

Figure 26: Evaporation of water within the hydrogel leads to regions dry polymer on the sample ends (opaque) while the middle length remains swollen (white).

With samples prepared following the previously described procedure, meniscus tracking experiments were conducted as described in Section 2.2 The purpose of these experiments was to explore how the meniscus velocity would change from the sections with dry PNIPAM to the section with swollen PNIPAM. As indicated by Figure 27, there was observed a sudden and significant change in slope (corresponding to water penetration velocity) between the dry and swollen regions. In Figure 27a, going from left to right, the slope changes from ~0.019mm/s to ~0.98mm/s, and drops back down to ~0.032mm/s in the last segment of dry polymer. The data in Figure 27a was obtained using the sample pictured in Figure 26, with the sharp transitions in slope corresponding to the red demarcations in that figure. For Figure 27b, the slope (i.e., velocity) changes from 0.75mm/s to 20.9mm/s, and then drops down to 4.93mm/s. These results indicate that contact line pinning is not due to presence of PNIPAM hydrogel, but rather to the presence of *dry* hydrogel.

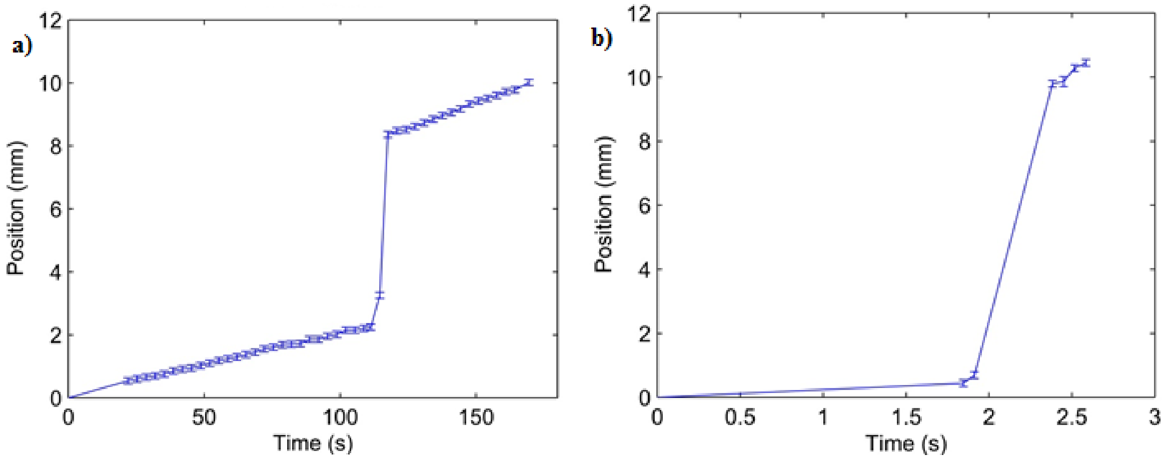

Figure 27: Meniscus position based on capillary action for (a) 300μm sample (b) 750μm ID gated samples. The sharp changes in slope are indicative of transitions from dry to swollen hydrogel, and vice versa.

3.4 Scaling Analysis for Contact Line "Stick-and-Slip"

As reviewed in Section 1.4.2, Kajiya *et al*. [46] explored contact line pinning for droplets placed on a dry film of swelling hydrogel. As part of the study, they employed scaling arguments in order to analyze factors governing the time to unpin the contact line. The same conceptual framework is adopted here, but modified for the capillary geometry.

3.4.1 Scaling Analysis Assumptions

By definition, a hydrogel is a 3D polymer network which has imbibed water. Thus, by assuming the incompressibility of both water and polymer, it becomes apparent that the volumetric change of the hydrogel due to swelling is exactly equal to volume of water which has entered the hydrogel.

Additionally, typical treatments of contact line motion feature one of two cases: 1) motion of a three-phase contact line in which the liquid displaces some vapor, or 2) motion of a three-phase contact line formed by the interface of two immiscible liquids (e.g., water and oil). While the swelling of the PNIPAM hydrogel introduces some complexity due to the diffusion of water into the gel to induce swelling, two distinct timescales (detailed in Section 3.4.2) allow the problem to be divided into two separate parts. During “stick” events, the contact line is pinned, and the analysis in the next section allows for insight as to how the meniscus profile and gel interface evolve as swelling occurs. In subsequent “slip” events, the contact line slips forward at a timescale later shown to be much faster than the characteristic swelling time. As a result, swelling and related mass transfer effects are decoupled from motion of the contact line, simplifying analysis.

3.4.2 Stick-and-Slip Model

Based on the high magnification meniscus position plots presented in Figure 20, it was postulated that the motion of the contact line through the gated capillary is a repeated sequence of stick and slip events outlined in Figure 28. Figure 28a depicts the pinned contact line, with the grey area representing dry hydrogel and the green area representing swollen hydrogel; R is the inner radius of the bare capillary; and $a(t)$ is the radial distance from the center line of the capillary to the swollen gel interface. As the contact line is pinned, water diffuses into the dry gel to initiate swelling. The swelling of the hydrogel in turn gives way to two characteristic angles: θ_{gel}, the angle between the axially extended gel slope and the contact line, and θ_{m}, the meniscus contact angle. As swelling continues, the contact line remains pinned as deformation of the gel causes θ_{gel} to increase as θ_{m} decreases (Figure 28b). In their work with planar samples (see Section 1.4.2), Kajiya *et al.* defined contact angle hysteresis $\Delta\theta$ to be $\Delta\theta = \theta_{\mathrm{gel}} - \theta_{\mathrm{m}}$. Since equilibrium contact angles on swollen gels were observed to be nearly 0°, Kajiya *et al.*

concluded that the contact line unpinned at $\theta_{\mathrm{gel}} = \theta_{\mathrm{m}}$ because this corresponds to $\Delta\theta = \theta_{\mathrm{gel}} - \theta_{\mathrm{m}} = 0°$. Likewise, since the PNIPAM films synthesized in this work were shown to have small contact angles in their swollen state (Chapter 4, Figure 33a), it was hypothesized that the contact line in the gated capillary would unpin upon $\theta_{\mathrm{gel}} = \theta_{\mathrm{m}}$, slipping over a distance L equal to the lateral deformation of the hydrogel beyond the contact line (Figure 28c). After traveling the distance L, the contact line re-encounters dry, undeformed PNIPAM and the process repeats, resulting in a repeated “stick-and-slip” sequence.

Regarding the value of L, there are two factors which can determine this length scale: axial diffusion of water from swollen to dry gel, and elastic deformation due to swelling of upstream gel (i.e., that which is in contact with bulk water). The extent of lateral deformation due to diffusion can be approximation by the diffusion length scale, $L_{\mathrm{diff}} \approx \sqrt{Dt}$. To place a conservative estimate on the time scale, let $t = 1$s (i.e., the time it takes a layer of hydrogel to swell to its equilibrium thickness). Taking $D = 5 \times 10^{-9} \frac{\mathrm{m}^2}{\mathrm{s}}$ (Appendix B) gives $L_{\mathrm{diff}} \approx 70$μm. To estimate L_{elas}, an analogy can be drawn to the problem of contacting elastic bodies [58], which details the extent to which a surface deforms in response to a fixed, local displacement. As shown in Figure 28, lateral forces acting on the hydrogel are unbalanced only in the region characterized by the meniscus depth, $h(t)$. Borrowing from the theory of contacting elastic bodies, L_{elas} therefore scales as $h(t)$, with $h(t) = a(t)(\csc\theta^* - \cot\theta^*)$ from sphere cap geometry. Since $a(t) \approx R$ due to thin hydrogel layers, $L_{\mathrm{elas}} \sim R$. Finally, since $L_{\mathrm{elast}} > L_{\mathrm{diff}}$ even in the conservative estimate for t_{diff}, $L \sim L_{\mathrm{elas}} \sim R$. In Figure 28, this elastic deformation is shown as the deformation of the dry gel from its nominal thickness (indicated by the dashed black lines).

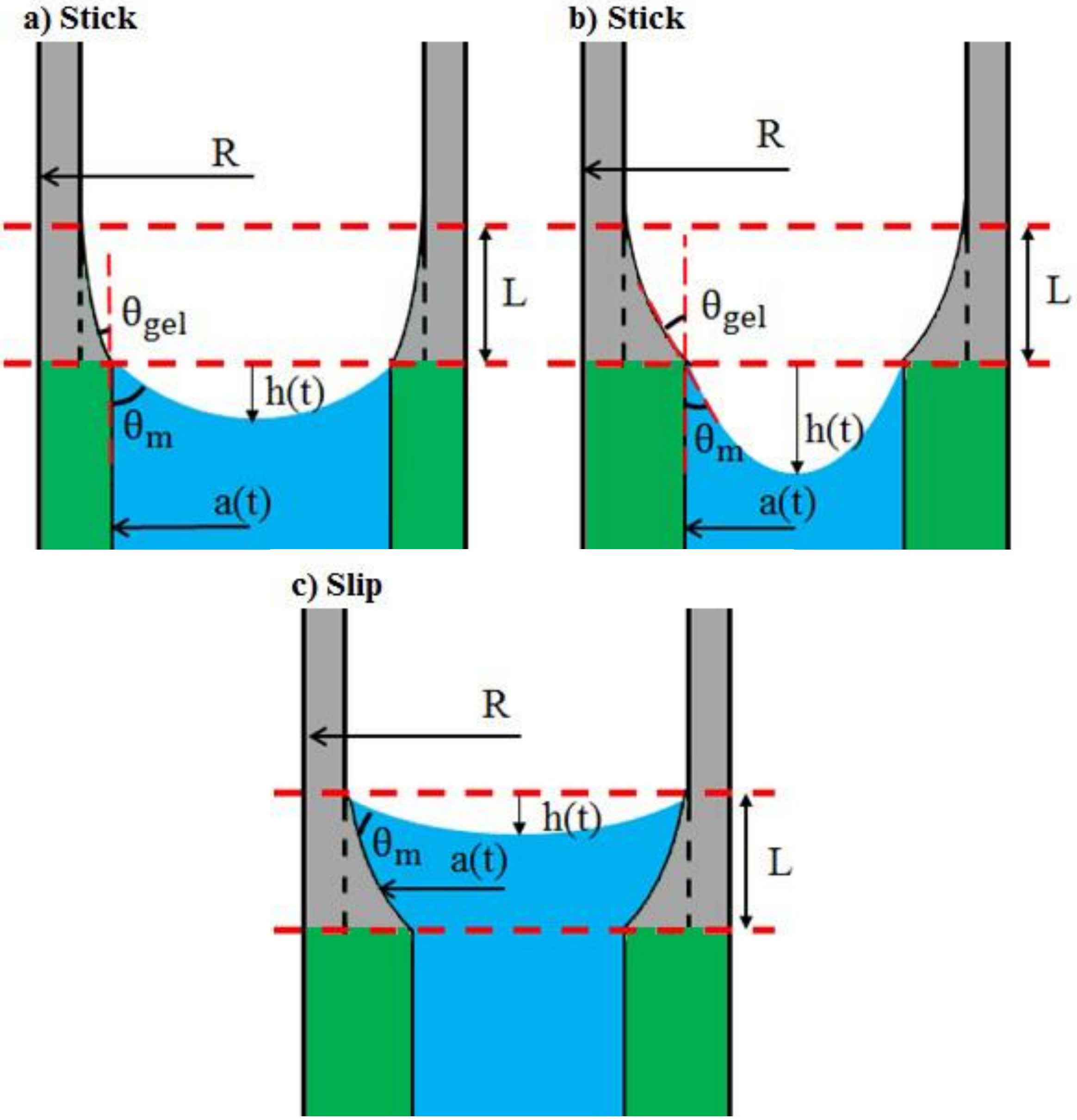

Figure 28: Contact stick-slip events; grey indicates dry gel while green indicates swollen gel. (a-b) Swelling of the hydrogel causes θ_{gel} and θ_{m} to evolve until they are equal. (c) Once this condition is met, the contact line slips forward over a distance L.

To supplement this qualitative description contact line motion, scaling analysis is employed in order to capture the evolution of θ_{gel} and θ_{m} during the time in which the gel is pinned. Due to the thin nature of these gel layers and for the purpose of simplifying analysis, the radius to the gel interface, $a(t)$, is assumed constant over the length L. Furthermore, the mass of the hydrogel can be written as $m_{\text{gel}} = m_p + m_w$, where m_p is the mass of polymer in the hydrogel (constant with time) and m_w is the mass of water in the hydrogel (variable with time). Accounting for the expansion of the layer depicted in Figure 29a,

$$\frac{dm_{\text{w}}}{dt} = -2\pi a(t)\frac{da(t)}{dt}L\rho_w \qquad 11$$

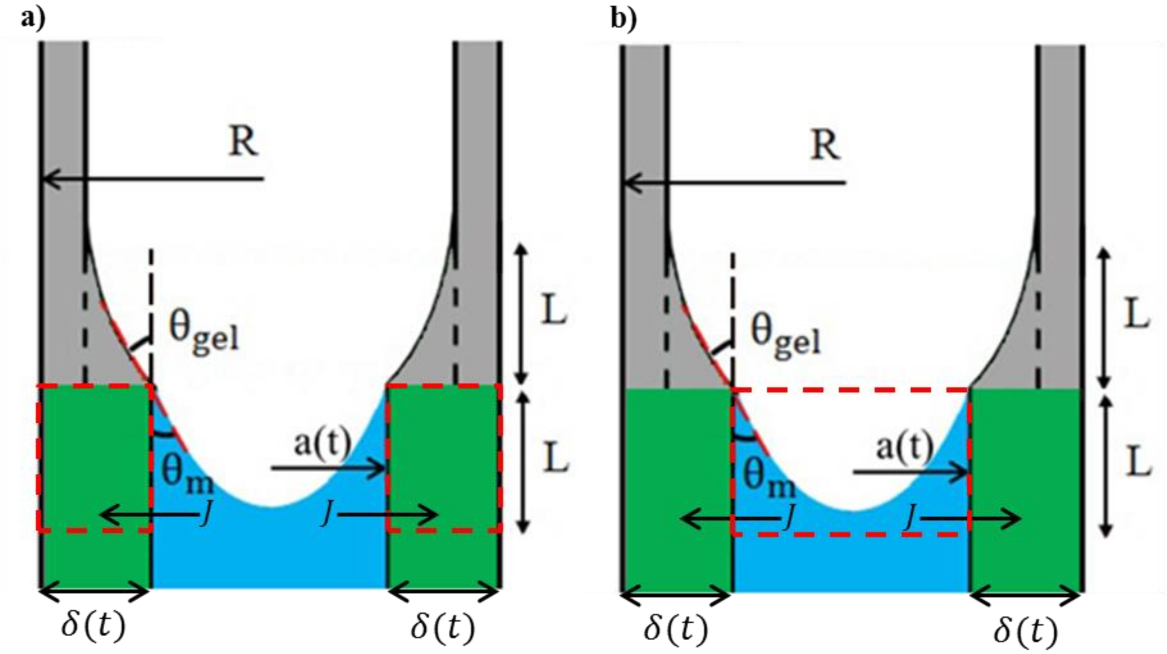

Figure 29: Designated control volume for conservation of mass analysis: (a) the swelling hydrogel layer, and (b) the bulk fluid.

Here, ρ_w is the density of water, while the minus sign accounts for the fact that the thickness of the gel layers increases at the same rate at which $a(t)$ decreases. By conservation of mass, this change in mass must be equal to the flux of water into the gel,

$$\frac{dm_{\text{gel}}}{dt} = 2\pi JLa(t) \qquad 12$$

where J is the mass flux of water into the gel. J is scaled as

$$J \sim D\rho_{\mathrm{w}} \frac{(\varphi_{\mathrm{sw}} - \varphi_{\mathrm{i}})}{\sqrt{\pi D t}} \qquad 13$$

Here D is the diffusion coefficient of water into the gel, φ_{sw} is the volume fraction of water in a swollen hydrogel (the water/gel interface is assumed to be instantaneously swollen), and φ_{i} is the volume fraction of water in the hydrogel in its initial state. The term in the denominator, $\sqrt{\pi D t}$ is the characteristic diffusion length scale, and provides a first-level approximation over which to calculate the effects of the effective concentration difference given by $(\varphi_{\mathrm{sw}} - \varphi_{\mathrm{i}})$. Combining Equations 11 and 12,

$$\frac{-da(t)}{dt}\rho_{\mathrm{w}} \sim J \qquad 14$$

θ_{gel} can be related to $a(t)$ by the estimation for the local slope $\tan(\theta_{\mathrm{gel}}) \sim {}^{\delta(t)}/_{L}$, where $\delta(t)$ is the thickness of the swollen gel layer. Since $\theta_{\mathrm{gel}}(t)$ is known to start at 0° and expected to vary within a 30-40° range, a small angle approximation can be applied, giving $\tan\theta_{\mathrm{gel}} \sim \theta_{\mathrm{gel}}$. Thus,

$$\frac{d\theta_{\mathrm{gel}}(t)}{dt} \approx \frac{1}{L}\frac{d\delta(t)}{dt} \approx -\frac{1}{L}\frac{da(t)}{dt} \qquad 15$$

Again, the minus sign arises from the fact that the rate of change of gel thickness is equal to $-a(t)$.

Combining Equations 13, 14, and 15, substituting $L = R$, and applying the initial condition $\theta_{\mathrm{gel}}^{0} = 0°$ gives $\theta_{\mathrm{gel}}(t)$:

$$\theta_{\mathrm{gel}}(t) \sim \frac{2}{R}\sqrt{\frac{Dt}{\pi}}(\varphi_{\mathrm{sw}} - \varphi_{\mathrm{i}}) \qquad 16$$

To determine $\theta_{\mathrm{m}}(t)$, assume that the change in mass of the bulk water (indicated in Figure 29b) is due only to mass flux of water into the hydrogel. Strictly speaking, the evolving meniscus profile ($\theta_{\mathrm{m}}(t)$ and $a(t)$ decreasing) means that there should be an external mass flux of water into this element as increasing curvature causes liquid pressure at the interface to decrease (Figure 31). For now, this external mass flux of water is assumed negligible in comparison to the mass flux of water to the hydrogel; the validity of this assumption is assessed at the end of this section. Thus, the change in mass of bulk water must be equal and opposite to the change in the hydrogel's water mass. Referencing Figure 29b,

$$V_{\mathrm{bulk}} = V_{\mathrm{cyl}} - V_{\mathrm{sph-cap}} \tag{17}$$

$V_{\mathrm{cyl}} = \pi a(t)^2 L$ and $V_{\mathrm{sph-cap}}$ is the empty region outside the meniscus. The volume of this region is defined by a spherical-cap whose volume can be written as

$$V_{\mathrm{sph-cap}} = \frac{\pi}{6} a(t)^3 \left[3\tan\left(\frac{\theta^*}{2}\right) + \left(\tan\frac{\theta^*}{2}\right)^3\right] \tag{18}$$

Here, θ^* is the contact angle of the spherical-cap, and is related to θ_{m} by $\theta^* = 90° - \theta_{\mathrm{m}}$. Recasting Equation 17 to account for change in mass in the bulk liquid and again assuming the incompressibility of water,

$$\rho_{\mathrm{w}} \frac{dV_{\mathrm{bulk}}}{dt} = \rho_{\mathrm{w}} \left(\frac{dV_{\mathrm{cyl}}}{dt} - \frac{dV_{\mathrm{sph-cap}}}{dt}\right) \tag{19}$$

Given the previous assumption that the change in mass of the bulk water is equal to the mass flux from the bulk fluid to the hydrogel,

$$\rho_{\mathrm{w}} \frac{dV_{\mathrm{bulk}}}{dt} = -2\pi J L a(t) \tag{20}$$

In order to solve for $\theta^*(t)$, the expressions for $V_{\mathrm{bulk}}, V_{\mathrm{cyl}}$, and $V_{\mathrm{sph-cap}}$ are substituted into Equation 19. Since only $a(t)$ and $\theta^*(t)$ are functions of time, this gives

$$\begin{aligned}\frac{\pi}{4}a(t)^3\left[\sec\left(\frac{\theta^*}{2}\right)^4\right]\frac{d\theta^*}{dt} &= 2\pi a(t)\frac{da(t)}{dt}L \\ &-\frac{\pi}{2}a(t)^2\frac{da(t)}{dt}\left[3\tan\left(\frac{\theta^*}{2}\right)+\left(\tan\frac{\theta^*}{2}\right)^3\right] \\ &+2\pi a(t)LJ\end{aligned} \qquad 21$$

Equation 21 is an ODE with non-constant coefficients and was solved using MATLAB’s ode45 function (an implementation of the explicit Runge-Kutta (4,5) method) with the initial condition. Material parameters relevant to solving Equation 21 are provided in Appendix B. The result was then transformed to $\theta_{\mathrm{m}}(t)$ through the relationship $\theta_{\mathrm{m}}(t) = 90° - \theta^*(t)$. By plotting the solutions for both $\theta_{\mathrm{gel}}(t)$ and θ_{m}(t), their intersection gives the time to unpin. As Figure 30 shows, this time is approximately 1.8s for the 300µm ID samples, and 2.6s for the 750µm ID samples.

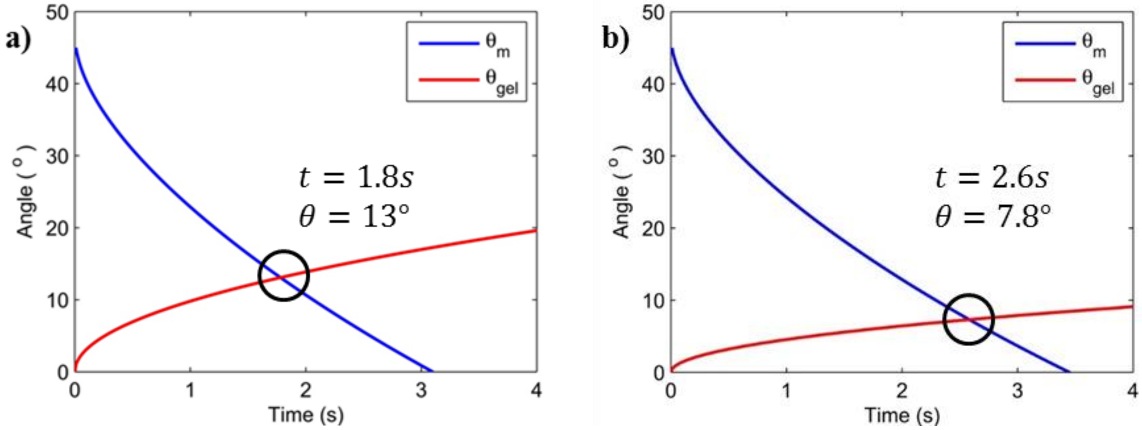

Figure 30: Evolution of $\theta_{\mathrm{m}}(t)$ and $\theta_{\mathrm{gel}}(t)$ for (a) 300µm ID gated capillary and (b) 750µm ID gated capillary for $\theta_{\mathrm{m}}^0 = 45°$.

As discussed previously, the physical mechanism driving this system is capillary pressure driven flow (which can be described by the Poiseuille equation). Once the contact line unpins, one can assume that the fluid flow obeys the Poiseuille equation for flow over the characteristic length L (i.e., Poiseuille flow occurs during the time that the fluid slips between stick events). Rearranging 7 to solve for the Poiseuille timescale as a function of the water meniscus position:

$$t_{\mathrm{slip}} = \frac{2x_{\mathrm{m}}^{2}\mu}{\gamma R \cos\theta} \qquad 22$$

In order to make a worst case approximation, one can calculate the time for the contact line to slip over the final length L (with L equal to the bare capillary inner radius) of the 1cm gated sample. Furthermore, assume that once the contact line slips, it slips with $\theta_{300\mu\mathrm{m}} = 13°$ and $\theta_{750\mu\mathrm{m}} = 7.8°$ (from Figure 30). From 22, this give $t_{\mathrm{slip}-300\mu\mathrm{m}} = 0.001\mathrm{s}$ and $t_{\mathrm{slip}-750\mu\mathrm{m}} = 0.0005\mathrm{s}$. While again, an argument can be made regarding the validity of the chosen contact angles, these slip times are orders of magnitude below the stick times reported seen in Figure 30. Because the stick time is constant and several orders of magnitude larger than the variable slip time, plots for meniscus position vs. time appear linear on a macro scale. However, by zooming in, on can find that this apparently linear behavior is actual a series of step events.

Since the timescales associated with the contact line slip are negligible, to compute t_{cap}, the time required for the contact line to penetrate the 1cm length of the gated capillary, is just a matter of scaling the stick time along the gated capillary length:

$$t_{\mathrm{cap}} = \frac{t_{\mathrm{pin}}}{L} \times 1\mathrm{cm} \qquad 23$$

Since the meniscus contact angle could not be observed inside the capillaries gated with PNIPAM, there existed some ambiguity as to the value of θ_{m}^{0}. Hence, Table 4 provides the variation in t_{cap} for different values of θ_{m}^{0}, and also calculates the ratio of t_{cap} for the 300μm ID samples to the 750μm ID samples. By averaging the time through the capillary for the experimental results presented in Figure 16, t_{cap} is 107±5s for the 300μm ID samples and 72±5s for the 750μm ID samples, giving a ratio of 1.49±0.12. Both the experimental values for t_{cap} and their ratio show good agreement with the predicted values, especially under the allowed margin for scaling analysis. Additionally, the scaling analysis captures the proper relationship between t_{cap} and R (namely, that t_{cap} decreases as R increases). Thus, the theoretical framework provided in this section appears to accurately capture the physics involved with contact line pinning in PNIPAM gated capillaries.

Table 4: Time to penetrate through capillary, for various values of the initial meniscus contact angle.

θ_{m}^{0}	t_{cap}: 300μm ID (s)	t_{cap}: 750μm ID (s)	Ratio
60	215	122	1.76
45	117	69	1.70
30	57	34	1.68
Experimental	**107 ± 5**	**72 ± 5**	**1.49 ± 0.12**

Based on Poiseuille theory alone, one would expect that the time for water to penetrate through a PNIPAM gated capillary would be greater for a smaller capillary inner diameter due to hydrodynamic resistance increasing with diameter to the fourth power. While the experimental data does follow this trend, the reason has nothing to do with hydrodynamic resistance because the Poiseuille timescale (i.e., slip) is negligible compared to pinning timescale (i.e., stick). While the 300μm ID gated capillaries do unpin faster than the 750μm ID gated capillaries, they also slip over a shorter distance. However, this is not likely a statement that can be applied to all cases given the relationships between key dimensions (gel thickness, capillary radius) and the scaling of relevant phenomena (diffusion vs. elastic deformation).

Looking back at Figure 20, plots Figure 20a and Figure 20b show a series of step like events associated with stick and slip. Though somewhat erratic, the jumps stick times in Figure 20a (750μm ID capillary) can be seen to range from 0.1 to 0.5s while jump lengths range from 10-70μm. In Figure 20b (also 750μm ID capillary), stick times can be seen to range from 0.15s to 0.6s while jumps fall between roughly 20μm and 60μm. In the limits of the scaling analysis, these distances are comparable to the assumed slip length of the capillary radius, and times are both roughly on the order as the calculated values. One change to the scaling analysis that could help to account for the differences would be to scale the slip length precisely as capillary depth $h(t)$ in Figure 28. While doing so would make L a function of θ_{m}, it could bring estimates closer to measured values. With regards to the absence of clear stick-slip behavior in Figure 20c and Figure 20d, it very well be that these stick timescales are on the order of what the camera can realize. Stick times of 0.1-0.5s were observed for the 750μm ID capillaries, and would be expected to decrease for the 300μm ID capillaries. Given the camera captures 1 frame every 0.03s, it would explain why stick/slip events are not as obvious in Figure 20c and Figure 20d.

In developing the governing system of equations, it was assumed that the time rate of change for the mass of bulk water is equal and opposite to the time rate of change of the gel water mass. Figure 31 shows the same control element as Figure 29b, but redrawn to include the mass flux resulting from the changing curvature of the meniscus. As mentioned previously, the swelling of the gel interface causes $\theta_{\mathrm{m}}(t)$ and $a(t)$ to both decrease. Since the capillary pressure goes as

$$\Delta P_c = \frac{2\gamma \cos(\,\theta_{\mathrm{m}}(t)\,)}{a(t)} \tag{24}$$

the capillary pressure increases as the contact line is pinned and the gel swells. This, in turn, causes the water pressure at the interface to decrease, leading to the mass flux into the control element (J_{in}). In order to estimate the value of $J_{\mathrm{in}}$and compare it to that of J (mass flux of water into the gel), it is possible to calculate $\dot{Q}_{\mathrm{in}}$ along L^{*}, the length scale

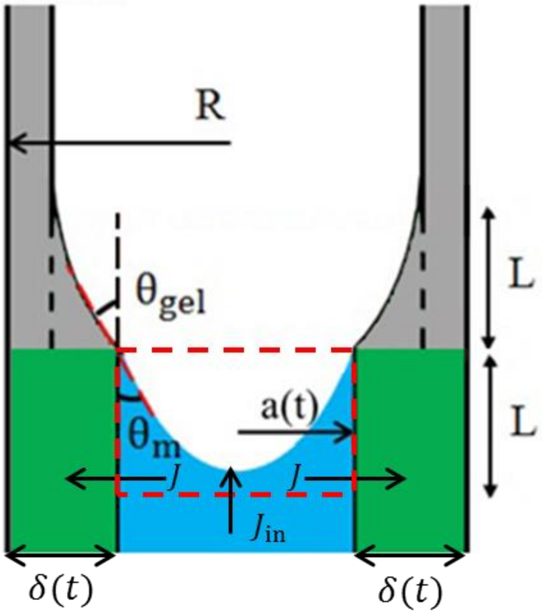

Figure 31: Modified schematic of Figure 29b, drawn to properly account for the mass flux of water into the control element due to the changing curvature.

upstream of the control element (Figure 32). Calculating $\dot{Q}_{\text{in}}$based on the assumption of Poiseuille flow from the capillary inlet to the control element,

$$\dot{Q}_{in} = \frac{\Delta P \pi (r_{\text{sw}})^4}{8\mu L^*} \qquad 25$$

with $J_{\text{in}} = \rho_w \dot{Q}_{\text{in}}$. In this approximation, the gel is assumed to be in its fully swollen state along L^*. Comparing J with $J_{\text{in}}$for $L^* = 1$mm (of the capillary sample's 1cm total length), $J_{\text{in}} \sim 1.2\text{ E} - 4\ {}^{\text{kg}}/_{\text{s}}$ while $J \sim 2.0\text{ E} - 2\ {}^{\text{kg}}/_{\text{s}}$. Since J_{in} decreases as L^* increases, J_{in} is shown to be negligible in comparison to J.

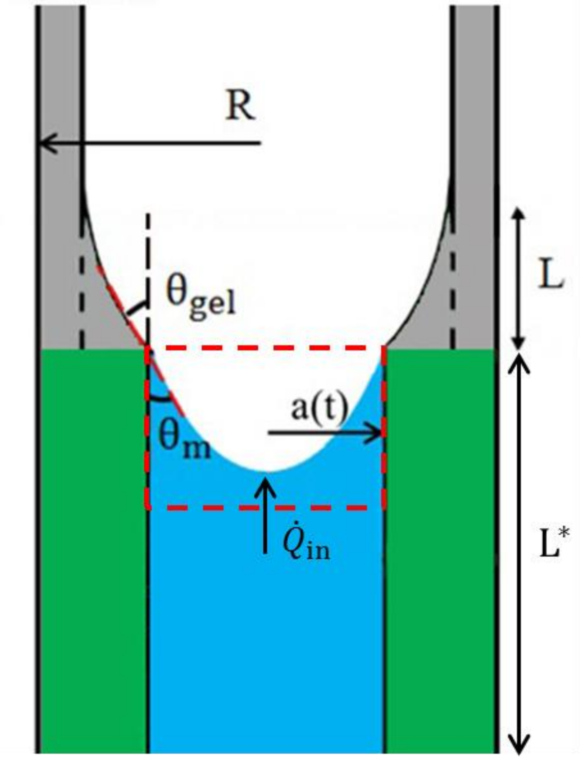

Figure 32: Estimation of bulk flow rate into control element by Poiseuille prediction.

3.5 Summary

The focus of this chapter was to demonstrate how swelling of PNIPAM hydrogels leads to localized pinning of the contact line during capillary driven flow. By initially presenting data for contact line motion under high magnification (200x), “stick-and-slip” behavior was observed in the experiments. This extra piece of information was important in demonstrating that the postulated contact line pinning was observable, and helped further substantiate the conclusions drawn at the end of Chapter 2.

Forced flow experiments showed good agreement between measured pressure drops and those calculated by Poiseuille predictions by considering the swollen PNIPAM layer as a modification to the capillary diameter. This revealed that the characteristic pipe resistance assumed in the Poiseuille equation could be applied to the case of water flow past PNIPAM layers, validating an implicit assumption in the analysis conducted in Chapter 2.

Furthermore, qualitative observations on the effect of polymer hydration on contact line dynamics further helped to support the idea of contact line pinning. Sample drying conditions between experimental runs were shown to have dramatic differences in the time to wick along a given length of gated capillary, likely as a result of entrained water. Samples that had been exposed to less rigorous dehydration conditions were likely left with trace amounts of water adsorbed to the surface, which then reabsorbed into the surface of the gel to reduce pinning effects during experiments. Likewise, water flow through samples with both dry and swollen segments of PNIPAM was shown to exhibit dramatic changes in contact line velocities in transitioning between these regimes.

Finally, these various results came together to postulate a physical mechanism that explains how evolution of key angles at the contact line manifested in a sequence of stick-and-slip events. The proposed mechanism was expressed mathematically using scaling analysis in order to compare characteristic times to wick through with PNIPAM gated capillaries with experimentally measured values. Results from this analysis showed good agreement with experimental values, and also captured the relationship between the capillary radius and the time for water to wick through.

Thus, it is concluded that swelling of PNIPAM hydrogel layers leads to a series of stick-and-slip motion as the contact line is continuously pinned and unpinned. Chapter 5 outlines possible future work related to this topic, while Chapter 4 will move into a different topic, exploring how PNIPAM nanorod array can be used for temperature modulation of surface wetting properties.

CHAPTER 4

EXPLORATORY WORK ON PNIPAM NANOSTRUCTURED SURFACES FOR TEMPERATURE-RESPONSIVE WETTABILITY

In discussing the shrinking/swelling behavior of PNIPAM hydrogel, there has been an implicit understanding that temperature changes above and below LCST affect the wettability of the gel. In this sense, phase separation of water above LCST can be seen as an increase in the polymer's hydrophobicity. Indeed, films of PNIPAM do exhibit temperature responsive wetting characteristics, as characterized by the difference in contact angle of deposited droplets (Figure 33).

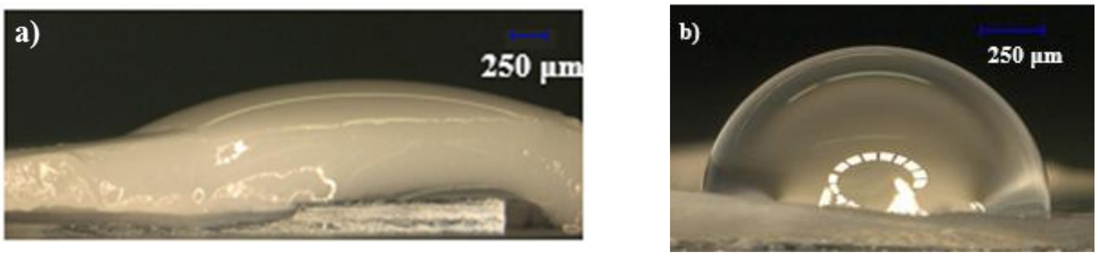

Figure 33: Droplet of water deposited on PNIPAM for (a) T < LCST and (b) T approaching LCST.

In years past, superhydrophobic surfaces attracted a great deal of attention due to the high contact angle droplets that formed on their surfaces. Associated with these high contact angles is increased droplet mobility, allowing for easy droplet/condensate removal and improve heat/mass transfer characteristics. Likewise, there are many potential applications for a surface with temperature-responsive wetting properties, and so the aim of this exploratory work was the creation of a PNIPAM nanostructured system that amplifies the hydrogel's natural wetting behavior. By nanostructuring a PNIPAM film, the effective nano-roughness would amplify the natural transition from hydrophilic to hydrophobic behavior upon heating (Figure 34).

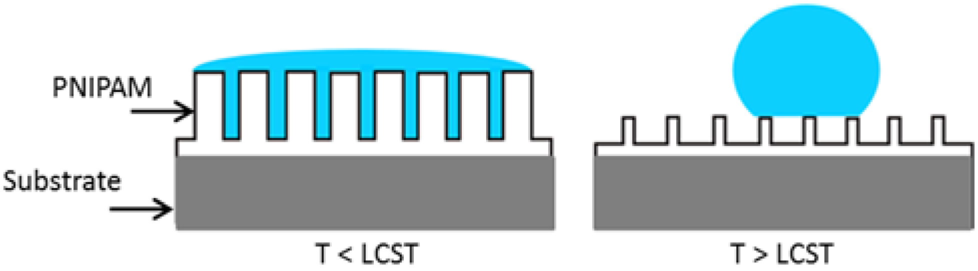

Figure 34: Target structure: a nanostructured PNIPAM film bonded to a hard substrate for handling. Nanostructuring the PNIPAM amplifies its intrinsic changes in wettability with temperature.

Desired characteristics of this nanostructured surface include:

- Amplification of intrinsic wetting properties of PNIPAM through introduction of nanoscale roughness
- Facile synthesis procedure via template-based methods, avoiding use of cleanroom-dedicated equipment
- Fast response to temperature shifts above/below phase transition LCST
- Reversible change in wetting behavior with long lifetime/stability

This chapter begins with a brief literature review of temperature responsive surfaces, and goes on to summarize results and lessons learned for a series of attempted fabrication techniques.

4.1 Thermo-Responsive Wetting

The primary body of work utilizing PNIPAM for temperature modulated wettability employs polymer chains grafted from a traditional “hard” surface (such as silicon). In these applications, the gel initiator is chemically bonded to the template surface, controlling points of polymerization and allowing for growth of chains [59-61]. In similar applications, a coating of PNIPAM was applied to a germanium nanostructure to impart temperature-responsive wettability [62]. In these cases, contact angles typically ranged from approximately 40-60° (at room temperature, below LCST) to 160° (above LCST) [56, 62]. However, in one case, by employing a two tier roughness system, Sun *et al.* were able to induce changes from superhydrophilicity to superhydrophobicity [57]. Their system featured nanoscale PNIPAM brushes grafted from microscale pillars laser etched into silicon, allowing droplet contact angles to change from roughly 0° (room temperature, below LCST) to 150° (above LCST).

While these applications of temperature-responsive surfaces have been reported in literature, in our work, we explore the use of PNIPAM hydrogel to form nanopillar structures, as opposed to polymer brushes.

4.2 Commercial Anodized Aluminum Oxide Templates

As a first attempt, commercial anodisc filters (anodized aluminum oxide, AAO) were purchased from Whatman Co. These filters were 1.3cm in diameter and had a rated pore size of 20nm. The idea was to use these filters as templates, casting PNIPAM nanopillars inside the porous structure, and then dissolving the template with aqueous NaOH in order to leave behind a nanopillar array.

To begin, the filters were silanized following the previously discussed method [47]. NIPAM precursor solution was then introduced by two different methods. In the first, the precursor solution was dropcast onto one side of the filter, allowing it to penetrate into the pores via capillary action. In the second method, filters were immersed in the precursor solution for several minutes. In both attempts, once it was believed that precursor solution had been drawn into the pores, the AAO template was lightly dabbed with filter paper in order to discourage formation of a gel film atop the porous disk (and thereby masking the internal porous structure). The filter was then placed in a furnace at 75°C and allowed to cure for 12 hours. After curing, filters were immersed in a 1M solution of NaOH for 30 seconds. The reason behind this short exposure time was to dissolve just a small portion of the AAO template, leaving enough AAO support material that the sample could be easily handled while also exposing only short PNIPAM nanorods. Following dissolution in NaOH, the AAO templates were thoroughly rinsed with DI water, dried, and sputtered with a 20nm layer of gold in order to aid imaging under scanning electron microscope (SEM).

For both methods pf introducing precursor solution into the AAO porouous structure, only minimal penetration of polymer into the porous structure was observed. Although the results presented in Figure 35 seemed promising, showing patches of nanopillars, they were confined to only a very small portion of the template. It is likely the difficulty in penetrating through the pores was due to branching in the porous structure of the commercial AAO filters used as templates. Since the commercial products were designed as size exclusion filters, only one side of the template needed to satisfy the rated pore size (Figure 36). As a result, 20nm pores on one side gave way to 200nm pores on the other, with a highly irregular structure in between. Branching and high degrees of irregularity inhibit filling and act to pin contact lines.

While effects of piranha cleaning and removal of the silanization step were explored, they did not improve the yield of nanopillars. Thus, it was concluded that while commercial templates were more convenient, their irregular branching patterns made them unsuitable for this process. As a result, homegrown porous alumina membranes were pursued as replacement templates.

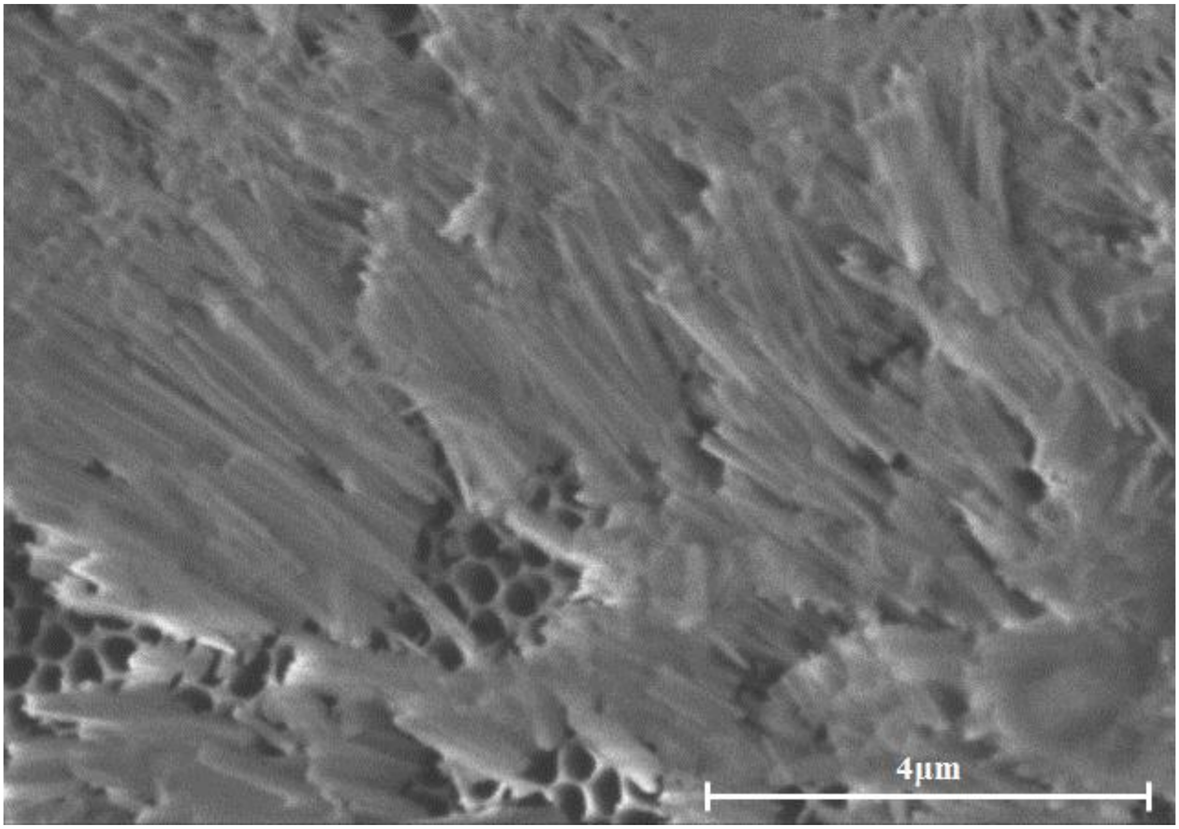

Figure 35: While use of commercial AAO filters as templates produced nanopillars, they were confined to a very small portion of the porous surface.

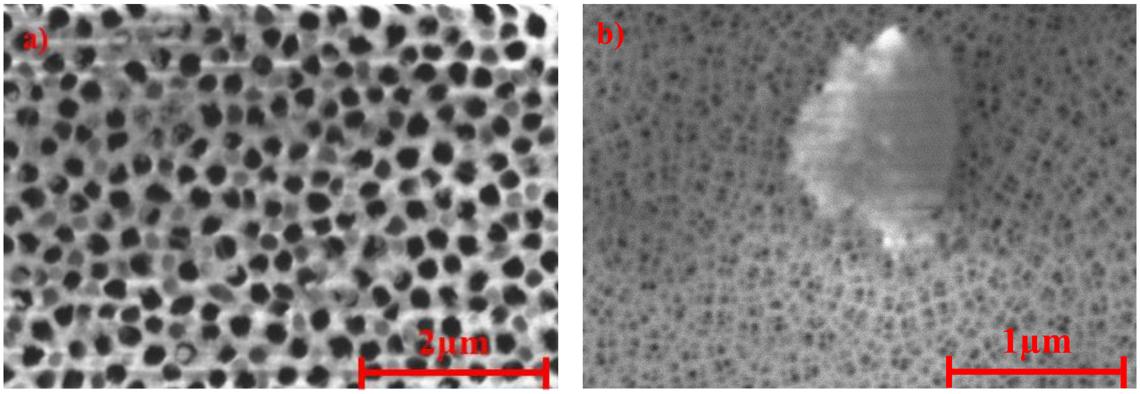

Figure 36: Whatman 20nm pore diameter filter. Inspecting the two sides of the filter under SEM, one side (a) shows pore closer to 200nm in diameter, while the other (b) has the rated 20nm pores.

4.3 Homegrown Porous Alumina Templates (With No Through Holes)

Due to the shortcomings attributed to the pore branching in the commercial samples, porous alumina templates were created in house. Given that creating the porous alumina templates followed a well-established procedure, an in-depth guide to the process as well as validation of the different steps can be found elsewhere [63]. What resulted from this process were silicon wafers (1cm x 1.5cm) with a 2µm thickness coating layer of porous alumina. Due to the process by which the aluminum was deposited and the pores were anodized, the pores were not through pores (Figure 37) as there existed a barrier layer before reaching the silicon. Nonetheless, the procedure demonstrated capability of producing straight, organized pores.

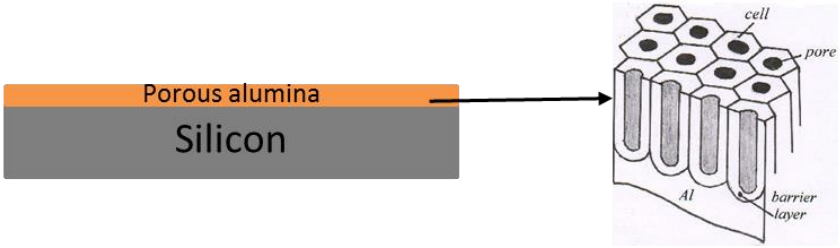

Figure 37: Homegrown porous alumina template. A 2µm layer of porous alumina rests atop a silicon wafer. While the pores are regular in structure, a barier layer separates them from the underlying silicon [64].

Initial experiments of fabricating PNIPAM nanostrcutures with the homemade porous alumina template followed the same procedure outlined in Section 4.2 of curing NIPAM precursor solution inside the template and then dissolving a top layer of the template to reveal the pillar structure. However, this approach still produced similar isolated patches of nanopillars as in Figure 35. Therefore, a modified approach was devised, in which rather than grow the nanopillars inside the porous structure, the porous alumina template would be used as a nano-stamp. As outlined in Section 2.1.2, it was found that when synthesizing planar PNIPAM gels of prescribed height, introducing a glass slide cover during curing forced the gel to take on the imposed shape. Removing the cover after 5 minutes allowed the gel to retain this imposed shape without bonding to the glass slide. Carrying over the same idea, NIPAM precursor solution would be deposited on silicon wafers with porous alumina templates were placed on top of the solution surface during curing in order to imprint the nanopillar shape. One approach had the porous alumina template held at a fixed height (Figure 38a), while another placed the template directly atop the solution (Figure 38b).

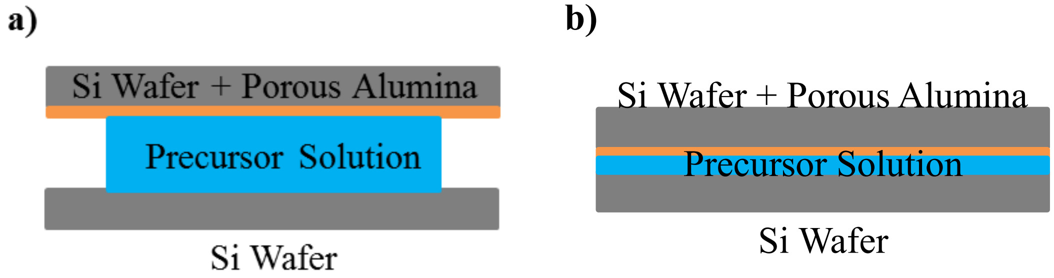

Figure 38: Using porous alumina templates to stamp nanostructured features: (a) template is held at a fiex height, vs. (b) template rests atop precursor solution.

While fixing the porous alumina template at a fixed height produced no noteworthy results, allowing it to sit under its own weight (Figure 38b) gave way to the profile pictured in Figure 39a. Though nanopillar coverage was not uniform across the sample, nanopillars were distinguishable. However, there was relatively little control over the process, as the thin layer of precursor solution would tightly bind the template to the target wafer, making them difficult to separate and inevitably damaging the sample surface in the process of template removal. Many of the nanopillars in Figure 39a agglomerated together, producing a sort of film-like material. As a result, a droplet deposited on the gel surface initially showed a hydrophobic contact angle of 110° (Figure 39b) before spontaneously assuming a lower contact angle around 90°.

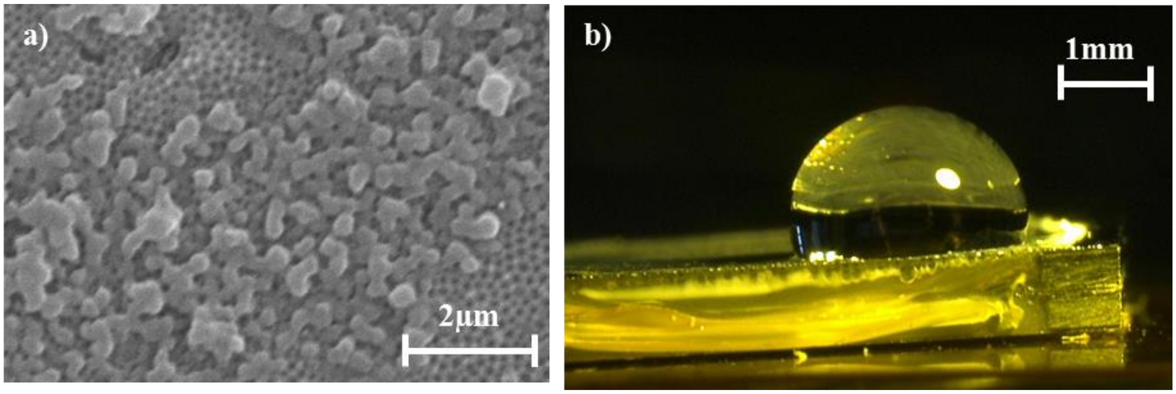

Figure 39: Results from nano-imprinting procedure outlined in Figure 38b.(a) PNIPAM nanopillars are present, but often agglomerate to give an irregular surface. (b) Water contact angle is approximately 110° on this surface upon initial deposition.

4.4 Homegrown Porous Alumina Templates (With Through Holes)

While the purpose of this exploratory work was to choose a synthesis route which avoided specialized cleanroom equipment, samples produced by such equipment were obtained that featured small areas of freestanding porous alumina. In these areas, well ordered pores spanned the sample thickness, eliminating the barrier layer pictured in Figure 37. To form the polymer nanopillars, precursor solution was dropcast on one side of the porous alumina and allowed to wick through under capillary action. Excess solution on the surface was cleaned with filter paper. After curing at 75°C, the sample was immersed in 1M NaOH for 30seconds to partially dissolve the porous alumina template.

As indicated in Figure 40 and Figure 41, having through pores seems to be the most essential feature for creating a regular nanoarray. Figure 40b reveals a nanopillar array of the same characteristic dimensions as the bare pores (Figure 40a), while Figure 41 shows that the formation of nanopillars covered large areas of the substrate and was not limited to patches on the surface as before. As one would expect, a through pore easily allows for transport of liquid throughout, making penetration much easier than in the previous two cases. Finally, analysis with atomic force microscope (AFM) reveals reasonable uniformaity of the surface (200nm or less variation in height), and is even able to resolve shapes of individual pillars (Figure 42).

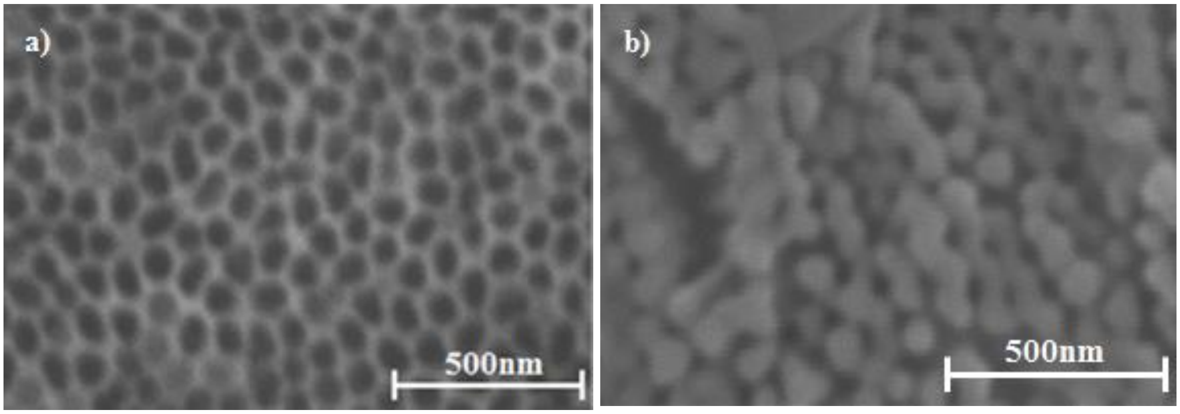

Figure 40: (a) SEM image of bare porous alumina template gives a pore size of 79±4nm. (b) After synthesis, partially dissolving the porous alumina template reveals PNIPAM nanopillars 80±4nm in diameter.

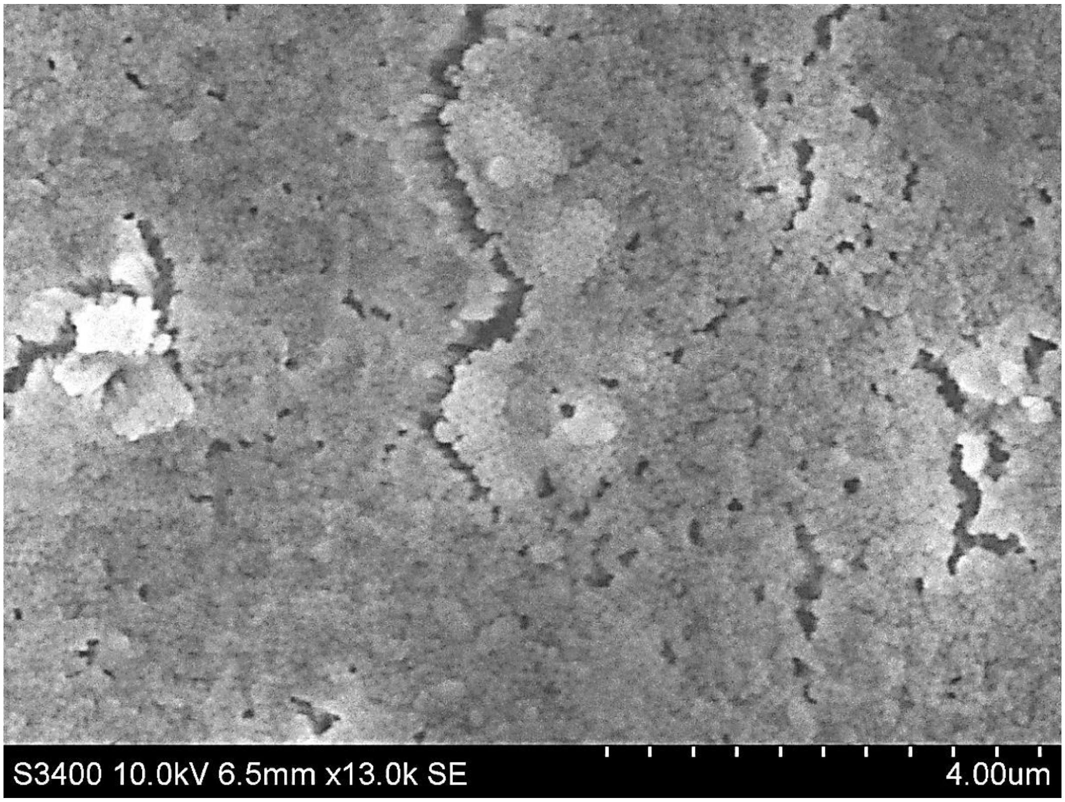

Figure 41: Regular array of PNIPAM nanopillars produced using freestanding porous alumina template with through pores.

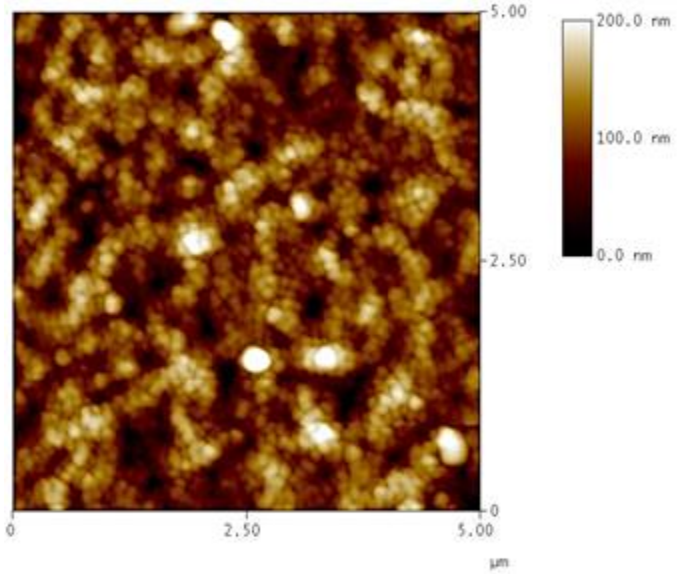

Figure 42: AFM profile of a5µm x 5µm nanopillar array.

4.5 Summary

In this chapter, several approaches were explored for creating PNIPAM nanopillar arrays. The main goal was to develop a technique for synthesizing the nanostructures in a typical lab setting, avoiding the need for specialized cleanroom equipment. Thus, using porous alumina templates emerged as a promising path for realizing this goal. The main obstacle encountered in this work was in forcing to NIPAM precursor solution to penetrate into the template pores. While methods pursued generally focused on creating favorable conditions for pore filling (i.e., use of capillary filling, immersion in solution), allowing a nano-stamp template to rest on precursor solution under its own weight improved penetration into pores across the template surface.

Based on the different synthesis techniques attempted in this thesis, results clearly indicated that a free standing porous alumina template with through pores delivered a regular array of PNIPAM nanopillars. Part of the reason for this could be the presence of a barrier layer at the end of a pore means that displaced gas will accumulate and pressurize as the pore is filled with precursor solution, thereby preventing complete penetration. Through, regular pores eliminate this issue, allowing the precursor solution to very easily penetrate through under capillary forces. The only potential issue in working with free-standing porous alumina templates is in transferring/adhering the nanostructured surface to a substrate. As with the case of the commercial templates, the current process requires partial dissolution of the freestanding template, leaving the bulk template behind for handling and supporting the nanostructured surface.

In working with porous alumina templates without through pores, next steps should focus on ways in which large pressure gradients can be forced across the porous alumina template in order to force liquid penetration. Such a technique would not have to run very long (application of a pressure differential over 30-60 seconds would likely be enough to force precursor penetration) and would distribute pressure uniformly across the template surface without tearing/removing hydrogel.

CHAPTER 5

CONCLUSIONS AND FUTURE WORK

5.1 Conclusions

Stimuli responsive polymers represent a unique material class capable of serving as both sensor and actuator for a wide variety of applications. With possible stimuli including temperature, pH, and electromagnetic fields, these polymers are currently the focus of many active research topics, and will likely begin to find widespread application, particularly in the biomedical field, in the coming years. For the numerous microfluidic applications which seek to employ swelling hydrogels such as PNIPAM as flow restriction elements, it is important to understand how water interacts with these swellings surfaces. As demonstrated in the literature review, analyzing contact line dynamics on swelling hydrogels is a problem that has only recently gained attention, and this was only for the case of planar samples.

A deal of time in this work was spent devising simple procedures for pre-treament of target substrates as well as synthesis of hydrogel layers. The synthesis methods devised avoid specialized equipment, and allow for straightforward application of these procedures for systems outside of gated capillaries. For instance, a logical extension of this work would be to synthesize PNIPAM coatings in channels with different geometries (e.g., triangular, rectangular, etc.) in order to assess the effects of these shapes on contact line dynamics.

Initially, contact line pinning in the PNIPAM gated capillary seemed completely counterintuitive- both glass and PNIPAM are hydrophilic at room temperatures, and yet introduction of a thin PNIPAM coating causes the time to penetrate through the capillary to increase by orders of magnitude. Nonetheless, repeated sets of meniscus tracking experiments confirmed that this behavior was not an isolated result. Thus, while exploring different possibilities for the mechanism causing such slow penetration times in the PNIPAM gated capillary, it became very important to establish experimental baselines along the way. For instance, by working with glycerol, it was shown that liquid penetration into the gated capillary did indeed follow Poiseuille predictions once the complexities introduced by hydrogel swelling were removed. Likewise, forced flow experiments revealed that a PNIPAM hydrogel coating does indeed follow predicted Poiseuille relationships for it characteristic hydraulic resistance, revealing that at the heart of this problem, pressure driven capillary flow is still responsible for fluid flow through the capillary.

By observing contact line behavior at high magnifications, contact line pinning was shown to be responsible for a series of “stick-and-slip” events that slowly propagated the contact line forward. These results were complemented by experiments which explored the effect of polymer hydration on contact line velocity, and found that partially and full hydrated segments exhibited significantly less pinning than completely dry segments. By recognizing that pinning was responsible for slowing the contact line, all of the physics in the problem could be captured by understanding a repeated sequence of events (giving rises to the observed linear relationship of meniscus position with time) that focused on evolution of the gel interface at the contact line.

To accompany schematic representations of postulated contact line pinning events, scaling analysis allowed for an analytical description of the problem. One advantage of this approach is that all of the parameters describing the derived equations for $\theta_{\mathrm{m}}(t)$ and $\theta_{\mathrm{gel}}(t)$ are in terms of measurable parameters (e.g. gel diffusivity, initial gel thickness, etc.). Although there was some initial ambiguity as to the value of θ_{m}^{0}, comparing the values of t_{cap} in Table 4 with the penetration times shown in Figure 16 indicates that θ_{m}^{0} should be between 30° and 45°. This range of values is consistent with that fact that the dry PNIPAM hydrogel is expected to be relatively hydrophilic at room temperatures, and gives more meaning to the value than in the case of initial Poiseuille models (where the contact angle was used as a fudge factor for fitting experimental data).

For the nanostructured PNIPAM surfaces, the exploratory work showed that templates with through holes deliver the desired result of a regular, well-defined nanopillar array. These promising results indicate the importance of through pores, and indicate that work should move in the direction of synthesizing free standing porous alumina templates (wherein synthesis of through pores should be relatively straightforward). Results from the use of a nano-stamp indicate that the synthesis route may be feasible if a large driving pressure can force better liquid impregnation of pores.

5.2 Future Work

One ongoing issue in working with capillaries is that the geometry, coupled with the opaque color of PNIPAM, limited experimental observation. Despite postulations as to how contact angles were evolving and how the gel was deforming, the only parameter that could be successfully measured was the position of the water meniscus. A possible workaround could be to synthesize the hydrogel on three sides of a square channel, leaving the fourth transparent and untouched. While having a fourth wall of a different material would change the problem by introducing surface/contact angle inhomogeneity, the setup could possibly allow for at least some visualization of contact line dynamics while still capturing the effects of the confined geometry.

Additionally, implementing a finite element model would help shed some light on the evolution of gel interface at the contact line in order to better understand the effects on pinning. While creating a model which successfully captures the relationships between bulk fluid motion in the capillary, gel deformation and water diffusion would be quite difficult, creating a model which focuses only on the latter two would be significantly easier. Such a model could be used to analyze individual pinning events (i.e., when the bulk fluid is stagnant) in order to better frame evolution key angles and the extent of lateral hydrogel deformation. Recently, Cai *et al*. formulated a 1D transient model for radial swelling of a gel disk [65]. A useful finite element model could be created by abstracting this work to the case of a 2D transient problem.

Lastly, repeating experiments with larger capillaries and thicker gel thicknesses would likely help to improve experimental results. While such changes would broaden the suite of results, they would also increase the timescales associated with swelling, producing more pronounced stick-and-slip behavior for the contact line

Assuming that synthesis of a PNIPAM nanopillar array is achieved (likely through the use of freestanding templates), an appealing concept would be to explore PNIPAM composite arrays. By simply mixing in ferromagnetic nanoparticles into the gel precursor solution, the particles would be trapped inside the gel matrix once curing occurs, making it very simple to go from a PNIPAM nanoarray to a composite PNIPAM nanoarray. In the case of magnetic nanoparticles, applied EM fields could be used to induce bending in the pillar structure (Figure 43). Doing so above LCST, when contact angles are quite high and droplets are especially mobile, could provide a mechanism for moving droplets in determined pathways, thereby rejuvenating the surface.

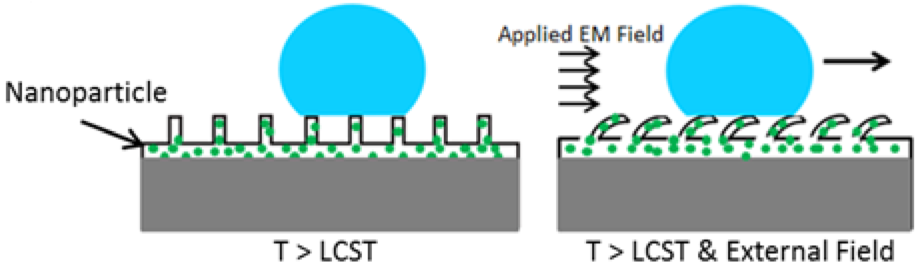

Figure 43: Integration of magnetic nanoaparticles into a PNIPAM nanopillar array. At T>LCST and with an applied EM field, bending of the nanopillars allows for transportation of the mobile droplet.

APPENDIX A

PIRANHA CLEANING PROCEDURE

1. Place substrates in a holder with slots that they can fit into. Place the holder in a large (~1L) beaker.
2. Fill the beaker with nanopure deionized water (18MΩ-cm resistivity) until all substrates are covered. Rinse twice. For capillaries, use a gas stream to force out entrained water between rinse cycles (applicable to all steps in which capillaries are rinsed).
3. Refill the beaker and place it in an ultrasonic bath. Set sonic timer for 10 minutes. Repeat twice.
4. Once sonication is finished, remove the water from the beaker and rinse the substrates two more times. Keep the beaker empty after the second time.
5. Transfer the beaker to a chemical hood, following all conventions for acid safety. Wear safety glass, acid-resistant apron, splash mask, and two pairs of gloves. Use caution.
6. Place the beaker (with the holder) inside a secondary container. The place the container in the chemical hood away from all other containers.
7. 300mL of piranha solution is needed in most situations (see Step 8 if cleaning capillaries). Unless the substrates are very large and require more solution, use only the smallest amount necessary. First pour 90mL of 30% H_2O_2 into the beaker. Then carefully add concentrated H_2SO_4 up to the 300mL line. Be aware that the solution will begin to boil. Cover the beaker with a sheet of aluminum foil.
8. For capillaries, it is essential to make sure that piranha solution uniformly fills the sample. In a small beaker, mix a solution that is 2:1 sulfuric acid to 30% H_2O_2, again keeping in mind that it will boil. Then, carefully add the capillaries to this solution, making sure to deposit one end first and allow filling via capillary action.
9. Wait one hour.
10. Carefully pour the waste piranha solution into the specially marked waste container. Clean up all spills using paper towels, and rinse paper towels thoroughly before disposing of them.
11. Rinse substrates five times with nanopure water.
12. Individually take the substrates from the holder and hold under a stream of dry gas at a shallow angle to dry. Remove all water droplets from the substrate.
13. Place the dried substrate in a clean glass (scintillation) vial.
14. Cover the holder and beaker with a new piece of aluminum foil and place in storage site.

APPENDIX B

MODEL PARAMETERS

<u>Hydrogel Diffusivity, *D*</u>

Several gated capillary samples were synthesized that featured PNIPAM coatings of sufficient thickness to fill the capillary cross-section upon swelling. Thus, when depositing a droplet at one end and allowing for capillary pressure driven flow, there would reach a point at which an entire length of capillary was filled with swollen hydrogel (Figure 44).

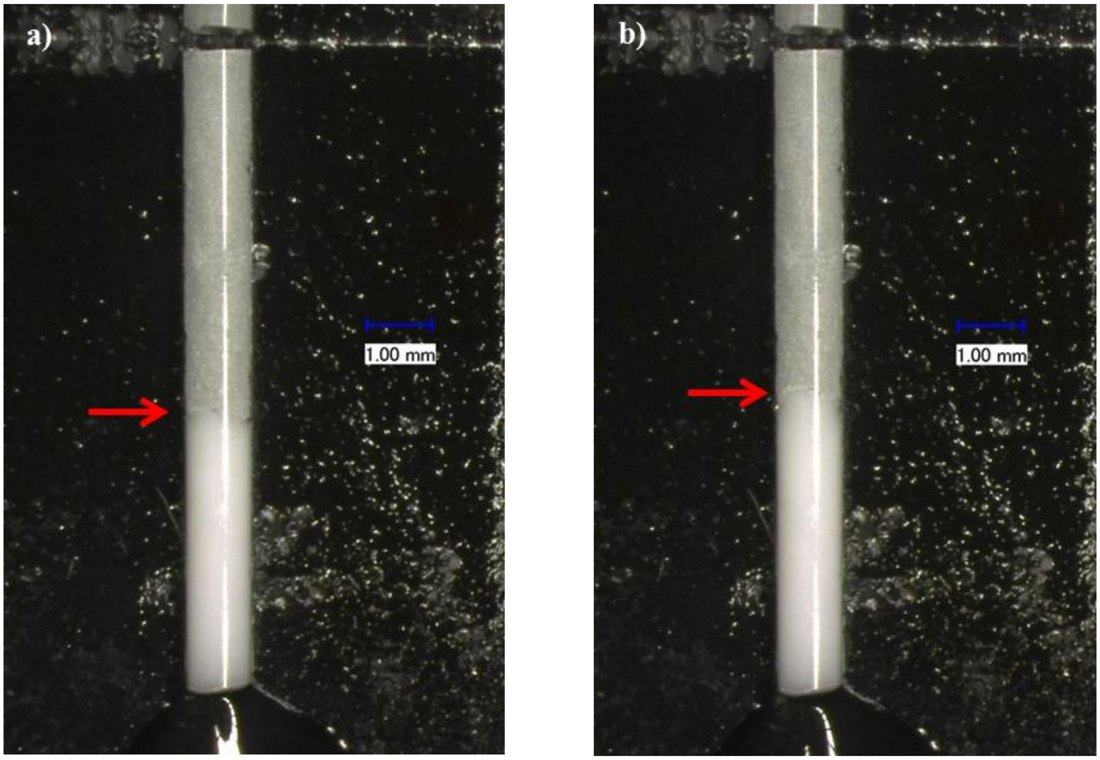

Figure 44: Meniscus position vs. time for a sample with PNIPAM that swells to fill the cross-section. Red arrows indicate meniscus position. (a) 300s and (b) 600s after reference time/position.

Based on the time and distance elapsed from a reference image (not pictured), the gel diffusivity was approximated as $\sim {L^2}/{t}$. This gave $\boldsymbol{D}\boldsymbol{\sim}\mathbf{1}\times\mathbf{10^{-10}}\,\mathbf{\frac{m^2}{s}}$ for three samples, which is consistent witch values reported in literature[66].

Gel Volume Fraction Difference

To calculate $\varphi_{\mathrm{sw}} - \varphi_{\mathrm{i}}$, swelling data was consulted in order to calculate the volume of dry hydrogel and the volume of imbibed water; due to incompressibility assumptions, it was assumed that $V_{\mathrm{swollen}} = V_{\mathrm{polymer}} + V_{\mathrm{water}}$. Table 1 gives characteristic dimensions for samples used. For scaling analysis, $\boldsymbol{\varphi}_{\mathbf{sw-300\mu m}} = \mathbf{0.32}$ and $\boldsymbol{\varphi}_{\mathbf{sw-750\mu m}} = \mathbf{0.37}$ ($\varphi_{\mathrm{i}} = 0$ in both inner diameter values).

REFERENCES

[1] D. Schmaljohann, "Thermo- and pH-responsive polymers in drug delivery," *Advanced Drug Delivery Reviews Advanced Drug Delivery Reviews*, vol. 58, pp. 1655-1670, 2006.

[2] Y. Zhang and A. L. Yarin, "Stimuli-responsive copolymers of n-isopropyl acrylamide with enhanced longevity in water for micro- and nanofluidics, drug delivery and non-woven applications," *Journal of Materials Chemistry,* vol. 19, pp. 4732-4739, 2009.

[3] Y. Lu, A. Zhuk, L. Xu, S. A. Sukhishvili, X. Liang, and E. Kharlampieva, "Tunable pH and temperature response of weak polyelectrolyte brushes: Role of hydrogen bonding and monomer hydrophobicity," *Soft Matter Soft Matter,* vol. 9, pp. 5464-5472, 2013.

[4] M. Zrínyi, "Intelligent polymer gels controlled by magnetic fields," *Colloid and Polymer Science*, vol. 278, pp. 98-103, 2000/02/01 2000.

[5] B. Ziolkowski, M. Czugala, and D. Diamond, "Integrating stimulus responsive materials and microfluidics: The key to next-generation chemical sensors," *Journal of Intelligent Material Systems and Structures Journal of Intelligent Material Systems and Structures,* vol. 24, pp. 2221-2238, 2013.

[6] S. Ghosh, A. Neogi, C. Yang, T. Cai, S. G. Mitra, D. Diercks, *et al.*, "Thermoresponsive Hydrogel Microvalve Based on Magnetic Nanoheaters for Microfluidics," *Materials Research Society symposia proceedings.,* vol. 1095, pp. 1-6, 2008.

[7] S. Rahimi, E. H. Sarraf, G. K. Wong, and K. Takahata, "Implantable drug delivery device using frequency-controlled wireless hydrogel microvalves," *Biomedical microdevices,* vol. 13, pp. 267-77, 2011.

[8] S. Purushotham and R. V. Ramanujan, "Thermoresponsive magnetic composite nanomaterials for multimodal cancer therapy," *Acta biomaterialia,* vol. 6, pp. 502-10, 2010.

[9] D. Subhash, H. Mody, R. Banerjee, D. Bahadur, and R. Srivastava, "Poly(N-isopropylacrylamide) based polymer nanogels for drug delivery applications," in *Nanotechnology (IEEE-NANO), 2011 11th IEEE Conference on*, 2011, pp. 1741-1744.

[10] A. Richter, S. Howitz, D. Kuckling, and K.-F. Arndt, "Influence of volume phase transition phenomena on the behavior of hydrogel-based valves," *Sensors and Actuators B: Chemical,* vol. 99, pp. 451-458, 5/1/ 2004.

[11] D. Kim and D. J. Beebe, "Hydrogel-based reconfigurable components for microfluidic devices," *Lab on a chip,* vol. 7, pp. 193-8, 2007.

[12] S. Ghosh, C. Yang, T. Cai, Z. Hu, and A. Neogi, "Oscillating magnetic field-actuated microvalves for micro- and nanofluidics," *Journal of Physics D: Applied Physics,* vol. 42, 2009.

[13] A. K. Lele, I. Devotta, and R. A. Mashelkar, "Predictions of thermoreversible volume phase transitions in copolymer gels by lattice-fluid-hydrogen-bond theory," *The Journal of chemical physics.,* vol. 106, p. 4768, 1997.

[14] Z. Hu, X. Zhang, and L. Y., "Synthesis and Application of Modulated Polymer Gels," *Science.*, vol. 269, p. 525, 1995.

[15] P. Chiarelli and P. Ragni, "Thermally Driven Hydrogel Actuator for Controllable Flow Rate Pump in Long-Term Drug Delivery," in *Biomedical Applications of Electroactive Polymer Actuators*, ed: John Wiley & Sons, Ltd, 2009, pp. 89-99.

[16] S. W. Hong, D. Y. Kim, J. U. Lee, and W. H. Jo, "Synthesis of Polymeric Temperature Sensor Based on Photophysical Property of Fullerene and Thermal Sensitivity of Poly(N-isopropylacrylamide)," *Macromolecules,* vol. 42, pp. 2756-2761, 2009/04/14 2009.

[17] C. D. Sorrell and M. J. Serpe, "Glucose sensitive poly (N-isopropylacrylamide) microgel based etalons," *Analytical and Bioanalytical Chemistry,* vol. 402, pp. 2385-2393, 2012/03/01 2012.

[18] D. I. Huber, R. P. Manginell, M. A. Samara, B. I. Kim, and B. C. Bunker, "Programmed adsorption and release of proteins in a microfluidic device," *Science (New York, N.Y.),* vol. 301, pp. 352-4, 2003.

[19] J. Wang, Z. Chen, M. Mauk, K.-S. Hong, M. Li, S. Yang*, et al.*, "Self-Actuated, Thermo-Responsive Hydrogel Valves for Lab on a Chip," *Biomedical Microdevices,* vol. 7, pp. 313-322, 2005.

[20] P. J. Flory, *Principles of Polymer Chemistry*. Ithaca: Cornell University Press, 1953.

[21] S. Cai and Z. Suo, "Mechanics and chemical thermodynamics of phase transition in temperature-sensitive hydrogels," *Journal of the Mechanics and Physics of Solids Journal of the Mechanics and Physics of Solids,* vol. 59, pp. 2259-2278, 2011.

[22] H. van der Linden, W. Olthuis, and P. Bergveld, "An efficient method for the fabrication of temperature-sensitive hydrogel microactuators," *Lab on a chip,* vol. 4, pp. 619-24, 2004.

[23] M. Guenther, G. Gerlach, C. Corten, D. Kuckling, M. Muller, Z. Shi*, et al.*, "Application of Polyelectrolytic Temperature-Responsive Hydrogels in Chemical Sensors," *MASY Macromolecular Symposia,* vol. 254, pp. 314-321, 2007.

[24] J. A. S. Seuring, "Polymers with Upper Critical Solution Temperature in Aqueous Solution," *Macromol. Rapid Commun. Macromolecular Rapid Communications,* vol. 33, pp. 1898-1920, 2012.

[25] C. Huh and L. E. Scriven, "Hydrodynamic model of steady movement of a solid/liquid/fluid contact line," *Journal of Colloid and Interface Science Journal of Colloid and Interface Science,* vol. 35, pp. 85-101, 1971.

[26] M. K. Andrews and P. D. Harris, "Damping and gas viscosity measurements using a microstructure," *Sensors & Actuators: A. Physical,* vol. 49, pp. 103-108, 1995.

[27] J. H. Snoeijer and B. Andreotti, "Moving Contact Lines: Scales, Regimes, and Dynamical Transitions," *Annu. Rev. Fluid Mech. Annual Review of Fluid Mechanics,* vol. 45, pp. 269-292, 2013.

[28] J. H. Snoeijer and J. Eggers, "Asymptotic analysis of the dewetting rim," *Physical review. E, Statistical, nonlinear, and soft matter physics,* vol. 82, 2010.

[29] T. Young, *An essay on the cohesion of fluids*. S.l.: s.n., 1804.

[30] R. N. Wenzel, "RESISTANCE OF SOLID SURFACES TO WETTING BY WATER," *Ind. Eng. Chem. Industrial & Engineering Chemistry,* vol. 28, pp. 988-994, 1936.

[31] A. B. D. Cassie and S. Baxter, "Wettability of porous surfaces," *Trans. Faraday Soc. Transactions of the Faraday Society,* vol. 40, 1944.

[32] C. W. Extrand and Y. Kumagai, "Contact Angles and Hysteresis on Soft Surfaces," *Journal of Colloid and Interface Science,* vol. 184, pp. 191-200, 12/1/1996.

[33] A. Carre, J.-C. Gastel, and M. E. R. Shanahan, "Viscoelastic effects in the spreading of liquids," *Nature,* vol. 379, pp. 432-434, 02/01/print 1996.

[34] L. Bacri and F. Brochard-Wyart, "Droplet suction on porous media," *The European Physical Journal E,* vol. 3, pp. 87-97, 2000/09/01 2000.

[35] C. Duprat, A. D. Bick, P. B. Warren, and H. A. Stone, "Evaporation of drops on two parallel fibers: influence of the liquid morphology and fiber elasticity," *Langmuir : the ACS journal of surfaces and colloids,* vol. 29, pp. 7857-63, 2013.

[36] J. Emile, A. Sane, H. Tabuteau, and O. Emile, "Experimental investigation of a moving contact line in a channel," *Soft Matter Soft Matter,* vol. 9, pp. 10229-10232, 2013.

[37] B. B. J. Stapelbroek, H. P. Jansen, E. S. Kooij, J. H. Snoeijer, and A. Eddi, "Universal spreading of water drops on complex surfaces," *Soft Matter,* vol. 10, pp. 2641-2648, 2014.

[38] T. Kajiya, A. Daerr, T. Narita, L. Royon, F. Lequeux, and L. Limat, "Advancing liquid contact line on visco-elastic gel substrates: stick-slip vs. continuous motions," *Soft Matter Soft Matter,* vol. 9, p. 454, 2012.

[39] T. Kajiya, P. Brunet, A. Daerr, L. Royon, T. Narita, F. Lequeux*, et al.*, "Wetting on Gels: How the Gel Characteristics Affect the Contact Line Dynamics," *Interfac Phenom Heat Transfer Interfacial Phenomena and Heat Transfer,* vol. 1, pp. 215-230, 2013.

[40] G. Pu and S. J. Severtson, "Characterization of dynamic stick-and-break wetting behavior for various liquids on the surface of a highly viscoelastic polymer," *Langmuir : the ACS journal of surfaces and colloids,* vol. 24, pp. 4685-92, 2008.

[41] G. Pu, J. Ai, and S. J. Severtson, "Drop behavior on a thermally-stripped acrylic polymer: influence of surface tension induced wetting ridge formation on retention and running," *Langmuir : the ACS journal of surfaces and colloids,* vol. 26, pp. 12696-702, 2010.

[42] D. Julkowska, M. Obuchowski, I. B. Holland, and S. J. Séror, "Branched swarming patterns on a synthetic medium formed by wild-type Bacillus subtilis strain 3610: detection of different cellular morphologies and constellations of cells as the complex architecture develops," *Microbiology (Reading, England),* vol. 150, pp. 1839-49, 2004.

[43] M. Banaha, A. Daerr, and L. Limat, "Spreading of liquid drops on Agar gels," *The European Physical Journal Special Topics,* vol. 166, pp. 185-188, 2009.

[44] D. Szabó, S. Akiyoshi, T. Matsunaga, J. P. Gong, Y. Osada, and M. Zrinyi, "Spreading of liquids on gel surfaces," *The Journal of Chemical Physics,* vol. 113, pp. 8253-8259, 2000.

[45] D. Kaneko, J. P. Gong, M. Zrínyi, and Y. Osada, "Kinetics of fluid spreading on viscoelastic substrates," *Journal of Polymer Science Part B: Polymer Physics,* vol. 43, pp. 562-572, 2005.

[46] T. Kajiya, A. Daerr, L. Royon, L. Limat, T. Narita, and F. Lequeux, "Dynamics of the contact line in wetting and diffusing processes of water droplets on hydrogel (PAMPS-PAAM) substrates," *Soft Matter Soft Matter,* vol. 7, pp. 11425-11432, 2011.

[47] B. Gorzolnik, P. Mela, and M. Moeller, "Nano-structured micropatterns by combination of block copolymer self-assembly and UV photolithography," *Nanotechnology,* vol. 17, pp. 5027-5032, 2006.

[48] J. Yoon, S. Cai, Z. Suo, and R. C. Hayward, "Poroelastic swelling kinetics of thin hydrogel layers: Comparison of theory and experiment," *Soft Matter Soft Matter,* vol. 6, pp. 6004-6012, 2010.

[49] S. A. Chester and L. Anand, "A coupled theory of fluid permeation and large deformations for elastomeric materials," *Journal of the Mechanics and Physics of Solids,* vol. 58, pp. 1879-1906, 2010.

[50] W. Hong, X. Zhao, J. Zhou, and Z. Suo, "A theory of coupled diffusion and large deformation in polymeric gels," *J Mech Phys Solids Journal of the Mechanics and Physics of Solids*, vol. 56, pp. 1779-1793, 2008.

[51] T. Komori and R. Sakamoto, "On Tanaka-Fillmore's kinetics swelling of gels," *Colloid and Polymer Science*, vol. 267, pp. 179-183, 1989/02/01 1989.

[52] T. Tanaka and D. J. Fillmore, "Kinetics of swelling of gels," *The Journal of Chemical Physics,* vol. 70, pp. 1214-1218, 1979.

[53] H. W. H. Poiseuille, *Experimental investigations upon the flow of liquids in tubes of very small diameter*. Easton, Pa, 1940.

[54] R. Tadmor and P. S. Yadav, "As-placed contact angles for sessile drops," *Journal of Colloid and Interface Science Journal of Colloid and Interface Science,* vol. 317, pp. 241-246, 2008.

[55] F. M. White, *Fluid mechanics*. Boston: McGraw-Hill, 2003.

[56] Q. Fu, G. V. Rama Rao, S. B. Basame, D. J. Keller, K. Artyushkova, J. E. Fulghum, *et al.*, "Reversible control of free energy and topography of nanostructured surfaces," *Journal of the American Chemical Society,* vol. 126, pp. 8904-5, 2004.

[57] T. Sun, G. Wang, L. Feng, B. Liu, Y. Ma, L. Jiang, *et al.*, "Reversible Switching between Superhydrophilicity and Superhydrophobicity," *ANIE Angewandte Chemie International Edition,* vol. 43, pp. 357-360, 2004.

[58] G. M. Hamilton, "Explicit expressions for the stresses beneath a sliding, spherical indenter," in *Proceedings of the Institution of Mechanical Engineers*, 1983.

[59] Q. Fu, G. V. R. Rao, L. K. Ista, Y. Wu, B. P. Andrzejewski, L. A. Sklar, *et al.*, "Control of Molecular Transport Through Stimuli-Responsive Ordered Mesoporous Materials," *Advanced materials.,* vol. 15, p. 1262, 2003.

[60] X. Liu, Q. Ye, Y. Liang, F. Zhou, X. Song, Y. Zhu, *et al.*, "Responsive wetting transition on superhydrophobic surfaces with sparsely grafted polymer brushes," *Soft Matter Soft Matter,* vol. 7, pp. 515-523, 2011.

[61] P.-F. Li, R. Xie, J.-C. Jiang, T. Meng, M. Yang, X.-J. Ju, *et al.*, "Thermo-responsive gating membranes with controllable length and density of poly(N-

isopropylacrylamide) chains grafted by ATRP method," *MEMSCI Journal of Membrane Science*, vol. 337, pp. 310-317, 2009.

[62] H. Ko, Z. Zhang, Y.-L. Chueh, E. Saiz, and A. Javey, "Thermoresponsive Chemical Connectors Based on Hybrid Nanowire Forests," *ANGE Angewandte Chemie*, vol. 122, pp. 626-629, 2010.

[63] S. Narayanan. (2011). *Gas assisted thin-film evaporation from confined spaces*. Available: http://hdl.handle.net/1853/42780

[64] (2012). *How and Why Alumina Matrix Architecture Influence the Shape and Composition of Nanowires Grown by AC Deposition?* Available: http://www.intechopen.com/articles/show/title/how-and-why-alumina-matrix-architecture-influence-the-shape-and-composition-of-nanowires-grown-by-ac

[65] S. Cai, Y. Hu, X. Zhao, and Z. Suo, "Poroelasticity of a covalently crosslinked alginate hydrogel under compression," *J. Appl. Phys. Journal of Applied Physics*, vol. 108, p. 113514, 2010.

[66] K. Takahashi, T. Takigawa, and T. Masuda, "Swelling and deswelling kinetics of poly(N-isopropylacrylamide) gels," *The Journal of Chemical Physics*, vol. 120, pp. 2972-2979, 2004.